

DEPENDENCE OF X-RAY BURST MODELS ON NUCLEAR REACTION RATES

R. H. CYBURT^{1,2}, A. M. AMTHOR³, A. HEGER^{2,4,5,6}, E. JOHNSON⁷, L. KEEK^{1,2,7,10}, Z. MEISEL^{2,8}, H. SCHATZ^{1,2,7},
AND K. SMITH^{2,9}

Draft version July 13, 2016

ABSTRACT

X-ray bursts are thermonuclear flashes on the surface of accreting neutron stars and reliable burst models are needed to interpret observations in terms of properties of the neutron star and the binary system. We investigate the dependence of X-ray burst models on uncertainties in (p,γ) , (α,γ) , and (α,p) nuclear reaction rates using fully self-consistent burst models that account for the feedbacks between changes in nuclear energy generation and changes in astrophysical conditions. A two-step approach first identified sensitive nuclear reaction rates in a single-zone model with ignition conditions chosen to match calculations with a state-of-the-art 1D multi-zone model based on the KEPLER stellar evolution code. All relevant reaction rates on neutron deficient isotopes up to mass 106 were individually varied by a factor of 100 up and down. Calculations of the 84 highest impact reaction rate changes were then repeated in the 1D multi-zone model. We find a number of uncertain reaction rates that affect predictions of light curves and burst ashes significantly. The results provide insights into the nuclear processes that shape X-ray burst observables and guidance for future nuclear physics work to reduce nuclear uncertainties in X-ray burst models.

1. INTRODUCTION

Type I X-ray bursts are the most frequently observed thermonuclear explosions in nature (Schatz & Rehm 2006; Strohmayer & Bildsten 2006; Lewin et al. 1993; Parikh et al. 2013). They take place on the surface of accreting neutron stars in low-mass X-ray binary systems for a certain range of mass transfer rates, generally within two orders of magnitude below the Eddington mass accretion rate ($\dot{M}_{\text{Edd}} \approx 2 \times 10^{-8} M_{\odot}/\text{yr}$; Woosley & Taam 1976; Joss 1977; Fujimoto et al. 1981; Strohmayer & Bildsten 2006). Since these events are not cataclysmic, bursts will repeat with recurrence times ranging from hours to days. The importance of understanding X-ray bursts as a probe of neutron star properties and the underlying physics has been discussed extensively (Lewin et al. 1993; Steiner et al. 2010; Zamfir et al. 2012; Özel 2013; Güver & Özel 2013).

The bursts are powered by the triple- α reaction, the ap -process and the rapid proton capture process (rp -process; Wallace & Woosley 1981; van Wormer et al. 1994; Schatz et al. 1998; Schatz et al. 2001; Fisker et al. 2008; Woosley et al. 2004; José et al. 2010). These nuclear processes involve hundreds of nuclear species from stable isotopes to the proton drip line. Models predicting burst light curves and the composition of the burst ashes are therefore sensitive to a broad range of uncertain nuclear structure and reaction properties near and beyond the current frontier of experimental knowledge. This limits interpretation of the vast body of observational data that has been accumulated (Galloway et al. 2008), for example in the MINBAR data base which will eventually contain X-ray light curve data of over 5000 X-ray bursts (Galloway et al. 2010).

Models with reliable nuclear physics are needed to validate the astrophysical model assumptions through comparison with observations, to guide future model developments towards an understanding of the full variety of observed bursting behavior, and to constrain parameters such as distance, accretion rate, accreted composition, and neutron star properties (Heger et al. 2007; Galloway et al. 2004). An example for the latter are recent attempts to constrain the neutron star surface gravity by matching a set of model bursts to observed light curves (Zamfir et al. 2012).

Whereas the X-ray light curve is the main direct observable of X-ray bursts, accurate nuclear physics is also needed to predict the composition of the burst ashes. Reliable calculations of this composition are required to predict potential spectroscopic signatures in the X-ray burst light curve from

¹ National Superconducting Cyclotron Laboratory, Michigan State University, East Lansing, MI 48824

² Joint Institute for Nuclear Astrophysics (JINA), <http://www.jinaweb.org>

³ Department of Physics and Astronomy, Bucknell University, Lewisburg, PA 17837

⁴ Monash Centre for Astrophysics, School of Physics and Astronomy, Monash University, Victoria 3800 Australia

⁵ School of Physics & Astronomy, University of Minnesota, Minneapolis, MN 55455, U.S.A.

⁶ Center for Nuclear Astrophysics, Department of Physics and Astronomy, Shanghai Jiao-Tong University, Shanghai 200240, P. R. China.

⁷ Department of Physics and Astronomy, Michigan State University, East Lansing, MI 48824

⁸ Department of Physics, University of Notre Dame, Notre Dame, IN 46556

⁹ Current Address: Oak Ridge National Laboratory

¹⁰ Current Address: CRESST and X-ray Astrophysics Laboratory NASA/GSFC, Greenbelt, MD 20771

small amounts of ejected material (Weinberg et al. 2006) and to predict the composition of the neutron star crust, which in mass accreting systems is made in part or entirely out of X-ray burst ashes. Of particular importance is the amount of ^{12}C , which may reignite at greater depth (Cumming & Bildsten 2001; Strohmayer & Brown 2002; Cumming et al. 2006) and explain the origin of occasionally observed superbursts (Keek & in't Zand 2008; Keek & Heger 2011). The thermal transport properties of the neutron star crust, as well as the amount of heating and cooling through weak interaction processes (Haensel & Zdunik 2008; Gupta et al. 2007; Schatz et al. 2014) also depend sensitively on composition.

The goal of this paper is to identify important reaction rates that affect observables and nucleosynthesis. Besides nuclear reaction rates, burst models also depend on β -decay rates and masses of neutron deficient nuclei. All relevant β -decay rates have been determined experimentally (Schatz & Rehm 2006), and corrections due to the high densities and temperatures reached in X-ray bursts are predicted to be small in most cases (Fuller et al. 1982; Pruet & Fuller 2003). However, the validity of these corrections remains to be evaluated in detail. The majority of the relevant nuclear masses has been measured as well. The impact of remaining mass uncertainties has been discussed elsewhere (Schatz 2006; Parikh et al. 2009; Kankainen et al. 2012). However, the rates for the vast majority of nuclear reactions occurring in X-ray bursts have not been determined experimentally and have large uncertainties. We therefore focus here on the sensitivity of X-ray burst models to nuclear reaction rates to provide guidance for future experimental efforts aimed at reducing the remaining nuclear physics uncertainties in X-ray burst models.

Comprehensive studies of the sensitivity of X-ray burst models to nuclear reaction rates have so far been limited to single-zone post-processing studies. Parikh et al. (2008) varied 3500 nuclear processes individually, and concurrently in a Monte Carlo approach, using fixed temperature and density profiles from various previously published X-ray burst models. An important result was the lack of additional sensitivities due to correlations among reaction rates in the Monte Carlo approach, justifying the single reaction rate variation approach to nuclear sensitivity studies for X-ray bursts that we also adopt here.

Post-processing studies with fixed temperature and density profiles, however, are not adequate to study nuclear sensitivities in X-ray bursts (Thielemann et al. 2001) because the entire reaction sequence contributes to the energy release driving the burst. Changes in reaction rates inevitably lead to changes in energy production, thereby to changes in the temperature and density evolution of the burst sequence. It is therefore essential to ensure consistency between the nuclear physics input and the

temperature and density evolution. Owing to computational limitations, however, sensitivity studies in fully self-consistent dynamic X-ray burst models have so far been limited to variations of a few individual reactions or a few groups of reactions. Thielemann et al. (2001) varied the proton capture rates on ^{27}Si , ^{31}S , ^{35}Ar , and ^{38}Ca together, rather than individually, in a 1D multi-zone X-ray burst model and demonstrated their strong influence on the light curve, in contrast to a post processing study that found these reactions to be unimportant (Iliadis et al. 1999). Fisker et al. (2004) varied the $^{30}\text{S}(\alpha, p)$ and $^{34}\text{Ar}(\alpha, p)$ reaction rates and demonstrated their impact on doubly peaked burst profiles. Woosley et al. (2004) varied groups of β -decay rates to simulate the potential impact of proton capture rate uncertainties on the burst light curve and found a very strong sensitivity. However, this only provides a crude estimate of how the overall processing speed of the rp-process may affect observables. It does not provide any insights into which proton capture rates may be important, nor whether proton capture rates are important at all. Fisker et al. (2006) determined a new lower limit of the $^{15}\text{O}(\alpha, \gamma)$ reaction rate and showed that bursts disappear altogether when that reaction rate is at that lower limit. Davids et al. (2011), however, did not find such an effect using a different X-ray burst model. More recently Keek et al. (2014) explored the impact of variations of the 3α , $^{15}\text{O}(\alpha, \gamma)$ and $^{18}\text{Ne}(\alpha, \gamma)$ reaction rates on the transition from unstable to stable burning in a multizone X-ray burst model.

Here we present a comprehensive study of the sensitivity of X-ray burst models to 1931 nuclear reaction rates using for the first time self-consistent X-ray burst models that account for the coupling between nuclear energy generation and the astrophysical conditions that determine the reaction sequences. Our approach is enabled by the use of two models. A calibrated, self-consistent one-zone model (Schatz et al. 2001) is used to explore variations of all reaction rates. A subset of relevant rates is then investigated further using a state-of-the-art 1D multi-zone burst model based on the KEPLER code (Woosley et al. 2004).

2. METHOD

In nature, the characteristics of X-ray bursts and the relevant nuclear reaction sequences vary between sources depending on accreted composition and neutron star properties, and even vary, for a given source, with time depending on the mass accretion rate. See Galloway et al. (2008) for a comprehensive overview of the range of observed burst properties and their dependence on source state, accretion rate, and accreted fuel composition. Lampe et al. (2015) provide a broad exploration of the impact of variations in astrophysical parameters on burst characteristics for the KEPLER burst model also employed here. We focus here on systems that accrete a mix of hydrogen and helium at high ac-

cretion rates, resulting in helium ignition in a mixed hydrogen and helium environment (burning regime 3 in Strohmayer & Bildsten 2006). Bursts in this regime are powered by the αp -process and the rp -process and exhibit extended burst tails. GS 1826-24 is the most studied source in this regime, and has served as a benchmark for X-ray burst models (Heger et al. 2007). Other sources in this regime are the low α high τ sources in Fig 14. of Galloway et al. (2008) with α being the ratio of energy released as persistent flux to energy released in bursts, and τ being the burst time scale.

To examine the effect of nuclear reactions we use the multi-zone hydrodynamics code KEPLER (Woosley et al. 2004). The full 1-D multi-zone model divides the envelope of the star into zones which have independent isotopic abundances. This allows the model to simulate burning processes and energy transport in full 1-D. In addition extended sequences of bursts are calculated where ashes from earlier bursts affect later ones, an effect known as compositional “inertia” (Taam 1980). KEPLER has been shown to reproduce the GS 1826-24 light curve reasonably well (Heger et al. 2007).

Full 1-D models require a large amount of computing time. We therefore use a single-zone model of Schatz et al. (2001) to first identify the most sensitive reactions and then determine the multi-zone model sensitivity to this subset of reactions. We have found that our single zone model approximates well the light curve and final composition calculated by KEPLER if the ignition conditions are chosen properly. Single-zone models that calculate changes of temperature and density conditions induced by changes in reaction rates self-consistently are more physical than a post-processing calculations, given that many reactions along the rp - and αp -processes affect the energy generation in X-ray bursts.

Our approach consists of the following steps: (1) We select ignition conditions for our one-zone model (pressure and composition) from among the conditions in the various zones of our KEPLER model just prior to the ignition of a typical burst (see below), such that the light curve and final composition agree as closely as possible with the KEPLER results. (2) We select a set of 1931 (p, γ), (α, γ), and (α, p) reactions along and near the reaction sequence in the one-zone model that spans the nuclear mass range of $A = 1-106$. (3) We vary each reaction, together with its inverse as determined by detailed balance, by a factor of 100 up and down and we rank reactions by their impact on the light curve and, in a separate ranking, on the composition. (4) We then vary the most important reactions in KEPLER, together with other reactions that have been identified as being important in X-ray bursts in the literature.

The factor 100 for the single zone variations was chosen as a worst case uncertainty to ensure no sensitivity is missed. This ensures we err on the inclusive side for the selection of reactions varied in

subsequent multi-zone calculations. Such large uncertainties can occur for reactions that are dominated by a small number of resonances (Clement et al. 2004) and were also found, as extreme cases, in comparisons of rates calculated with the theoretical Hauser-Feshbach approach (Rauscher & Thielemann 2000) (the majority of reactions investigated here) with experimental data (Parikh et al. 2013; Deibel et al. 2011). Even with these large variations, the number of reactions that cause significant light curve changes was still manageable. For the reaction rate variations in KEPLER we reduce the factor of variation in cases where the reaction rate error is likely to be much smaller. We emphasize that the goal here is not to provide a realistic uncertainty estimate but to identify important reactions. Variations are therefore chosen to overestimate rather than underestimate uncertainties to ensure identification of important reactions. Modifications to the light curve and composition for different variation factors may be roughly estimated using our results, if, for example a detailed analysis of reaction rate uncertainty is carried out in a particular case.

As baseline nuclear physics input, we adopt thermonuclear and ground state weak rates and the corresponding nuclide properties (e.g. masses and partition functions) from the snapshot library ReaclibV1.0 from the JINA REACLIB Database (Cyburt et al. 2010), the most up-to-date library at the beginning of this study. We also adopt temperature and density dependent weak rates from Fuller et al. (1982) and Pruet & Fuller (2003). Test calculations carried out with the rates from Oda et al. (1994) did not show any significant differences.

2.1. Multi-zone Model

The 1D multi-zone X-ray burst model used in this study is based on the hydrodynamics code KEPLER (Weaver et al. 1978), and is discussed in detail in Woosley et al. (2004). This model couples the energy generation of a complete, adaptive nuclear reaction network of over 1300 isotopes to a one-dimensional hydrodynamic simulation of the accretion on an adaptive Lagrangian grid, nuclear burning, radiative and convective energy transport, and mixing of the isotopic composition both during and between bursts. A “smooth” accretion scheme as well as an updated implementation of electron conduction are employed (Keek & Heger 2011). The radial dimension of the accreted layer is resolved into typically around 200 zones. The model follows a sequence of bursts taking into account steady state nuclear burning in-between bursts and compositional inertia effects, where ashes from preceding bursts partially mix with freshly accreted material and affect the nuclear processes in subsequent bursts.

The specific accretion model used for these studies is model ZM from Woosley et al. (2004), with solar metallicity material (hydrogen mass fraction $X = 0.7048$, helium mass fraction $Y = 0.2752$,

and ^{14}N mass fraction 0.0200) accreted at a rate of $1.75 \times 10^{-9} M_{\odot}/\text{yr}$, roughly 10% of the Eddington mass accretion rate. This model represents a typical burster powered by mixed hydrogen and helium burning producing longer bursts with timescales well beyond 10s, up to minutes (Galloway et al. 2004). A version of this model at slightly lower accretion rate produced the best agreement with observations to date (Heger et al. 2007).

The neutron star is taken to be 10 km in radius and to have a mass of $1.4 M_{\odot}$. Since this study involves no comparison to observational data, the general relativistic correction from the neutron star frame to an observer at infinity will be neglected (Woosley et al. 2004). All times are therefore given in the reference frame of the neutron star surface.

The multi-zone X-ray burst model was first run for a long sequence of bursts (~ 50) using the unmodified baseline reaction rate database, Reaclib v1.0. The long sequence of bursts serves as a baseline and ensures enough burst statistics to characterize steady state burst properties, including burst-to-burst variations that affect the identification of sensitivities to reaction rate changes. The models with varied reaction rates were run for shorter times for a set number of simulation timesteps. This limits the computational time needed for each run. Because the time step size in KEPLER is dynamically adjusted to optimally resolve the time-dependent behavior, the total simulation time varies among the multi-zone simulations. The multi-zone model calculations with individual reaction rate variations generally produced about 14 bursts, but in all cases, a continuous sequence of at least 12 bursts was simulated. This is sufficient to ensure convergence into a steady state bursting behavior.

The burst lightcurves are shown in Fig. 1 and Fig. 4. The first burst is special, because it occurs atop an inert neutron star substrate (assumed as iron for the purpose of heat conduction) though in this model it turns out to be quite similar to the following bursts. Already the second burst is very similar to the remaining bursts and there is no evidence for systematic variation beyond the second burst indicating that reasonable steady state equilibrium is achieved beginning with the third burst. At this point bursts occur rather regularly, with a recurrence time of $t_{\text{rec}} = 175 \pm 3$ minutes, peak luminosity of $L_{\text{peak}} = (1.7 \pm 0.1) \times 10^{38} \text{ ergs s}^{-1}$, and a total energy released during the burst, $E_{\text{tot}} = (6.5 \pm 0.1) \times 10^{39} \text{ ergs}$, (all numbers given in the local neutron star surface reference frame). The quoted uncertainties are standard deviations and stem from the remaining intrinsic burst-to-burst variations. These variations do not decrease with the number of bursts and are a feature of the steady state behavior of the model. In steady state, bursts have a rise time of $5.3 \pm 0.1 \text{ s}$ from 10% to 90% of L_{peak} , and a duration of $\tau = E_{\text{tot}}/L_{\text{peak}} = 39 \pm 3 \text{ s}$. The 10% (rise) to 10% (decline) luminosity burst duration is $73 \pm 5 \text{ s}$.

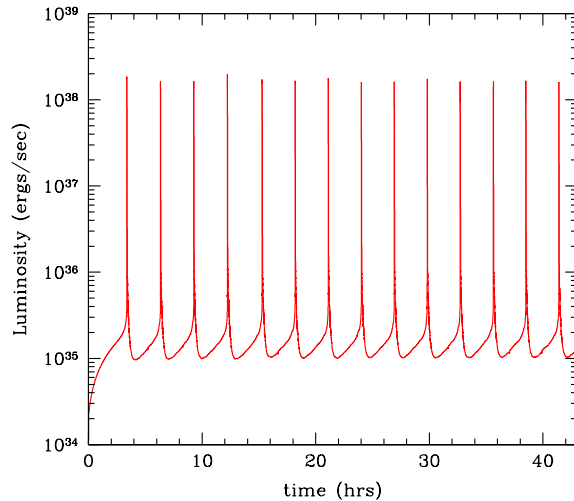


FIG. 1.— Luminosity as a function of time for the first 15 bursts of a burst sequence calculated with the multi-zone model. Note that this is only the luminosity from the neutron star itself, after accretion of the material; an observed XRB light curve would have the accretion luminosity of $2 \times 10^{37} \text{ erg/s}$ added.

In Fig. 4 the burst luminosity profiles are shown, shifted in time to align the peak luminosities of all bursts. Burst-to-burst variations not only affect recurrence time and peak luminosity, but also the shape of the light curve.

This study requires direct comparison of two light curve sequences calculated with different nuclear physics. The burst-to-burst variations need to be taken into account for this comparison. In order to define a light curve for comparison, we take the ensemble of bursts starting with the third burst, shift each burst to align the peak luminosity in time, and resample all bursts on a common time grid using linear interpolation. The surface resolution of our model is finer than what was used by Heger et al. (2007), with the mass of the outer zone being up to 100 times lower. At times when the burst is brightest, an individual zone near the surface may get a “kick”, and its behavior differs briefly from the rest of the outer zones. To prevent this from influencing the simulated light curve, we average the luminosity of the outer-most 9 zones and smooth over a scale of one second to remove any numerical noise. At each point in time we consider the variations in luminosity from all remaining bursts, and determine the average luminosity and its error. This average light curve with error band is used for our sensitivity study. Using an average is justified because observationally precise burst light curves can also be obtained by averaging long sequences of bursts (Galloway et al. 2004).

We also investigate the sensitivity of the steady-state burst ashes to nuclear reaction rate variations. This steady-state burst ashes of a burst sequence is determined in the following way: The deepest zones at the end of our multi-burst simulation sequence are special as they represent the ashes of the first bursts before a steady-state burst behavior was

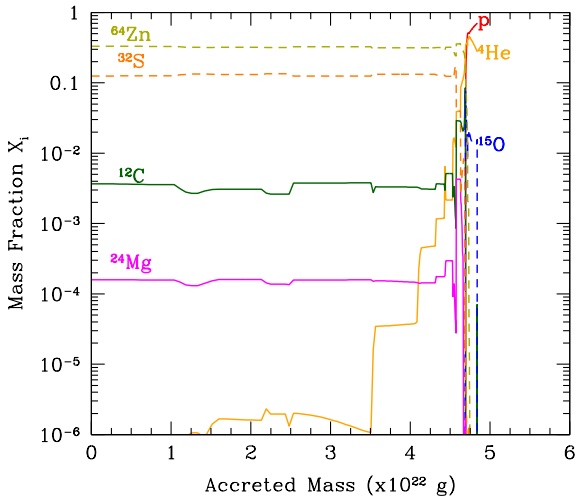


FIG. 2.— Average mass fraction of various nuclides as a function of accreted mass in the multi-zone model. Zero accreted mass marks the base of the accreted material. 4.8×10^{22} g corresponds to the surface and reflects the total accreted mass at the point in time shown.

achieved. Similarly to the procedure adopted for the light curves, we therefore remove ashes from the first two bursts from our analysis to prevent anomalous zones from contributing. Too-shallow zones also have to be excluded as they will continue to be modified by subsequent bursts and therefore do not represent the steady-state ashes. Clearly this includes zones that still contain hydrogen. Deep unburned helium, however, can also be burned during heating from bursts occurring in shallower regions (Woosley et al. 2004). This can be seen in Fig. 2 where the helium mass fraction successively decreases with increasing depth. As the helium mass fraction becomes lower, the modifications in the ashes induced by burning of residual helium become less important. We therefore exclude shallow zones with helium mass fractions above $\sim 3.0 \times 10^{-5}$ from the calculation of our final composition. For a typical burst model used with the reaction rate variations, these constraints result in an averaging of the final composition over a depth range of $M_{\text{acc}} \sim 3 - 6 \times 10^{21}$ g (see Fig 2). We chose the time (rounded to nearest 100^{th} time-step, as one in every 100 steps is stored) at which the light curve is minimum after the 12^{th} burst as our point for determining this composition.

Fig. 3 shows the resulting isobaric ash composition. The abundance peak around $A = 40$ stems from the impedance of the nuclear reaction sequence caused by the $Z = 20$ shell closure at the ^{40}Ca waiting point, whereas the abundance peaks around $A = 60 - 64$ are produced by the ^{60}Zn , ^{64}Ge , and ^{68}Se rp -process waiting points, which have particularly long half-lives despite being located at the proton drip line (Schatz et al. 1998). The NiCu and ZnGa cycles further enhance abundances in this mass region (van Wormer et al. 1994). The α -chain isotopes ($A = 12, 16, 20, 24, 28, 32$) are further enhanced by late helium burning once hydrogen is consumed. The time and zone integrated reaction flow

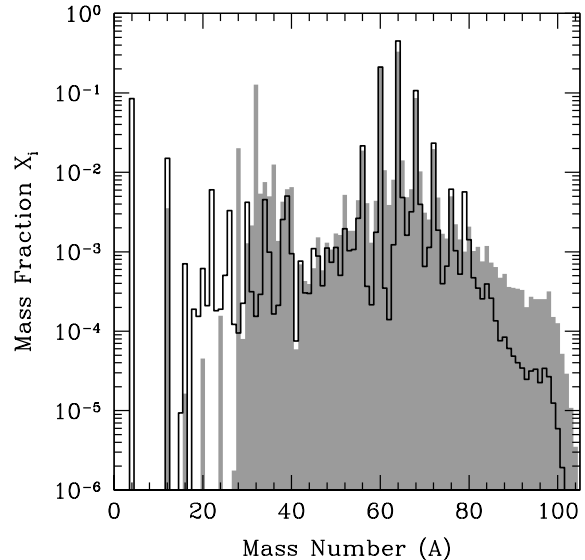


FIG. 3.— Steady state composition summed by mass number produced by a burst sequence in the multi-zone burst model (grey shaded histogram) and by the single-zone burst model (black line).

during a typical X-ray burst is shown in Fig. 13 to illustrate the type of reactions that occur.

2.2. Single Zone model

The one-zone model ONEZONE is similar to the model of Koike et al. (1999) and has been used previously to estimate the reaction sequence of the rp -process (Schatz et al. 2001). It evolves thermodynamic conditions and composition in a single zone, neglecting gradients in temperature, density, and composition, as well as radiative transport and convection. ONEZONE assumes nuclear burning at constant pressure P . This is justified, as mass accretion during the burst is negligible and only little material is ejected. As the burning happens in a thin layer on the surface, the influence of the neutron star is fully characterized through the surface gravity g (neglecting magnetic fields and rotation). The evolution of the temperature starting at burst ignition is calculated for a time step dt using $dT = c_P^{-1}(\epsilon_{\text{nuc}} + \epsilon_{\text{cool}} + \epsilon_{\nu})dt$ with the specific heat capacity at constant pressure c_P , the positive specific nuclear energy generation rate ϵ_{nuc} , the negative specific surface cooling rate ϵ_{cool} , and the negative specific neutrino loss rate ϵ_{ν} .

$$\epsilon_{\text{nuc}} = \frac{\sum_i dY_i \Delta_i}{dt} \quad (1)$$

is calculated from the abundance changes dY using atomic mass excesses Δ , assuming positrons emitted in β^+ decays are annihilated instantly. For X-ray burst conditions, ϵ_{ν} is entirely due to neutrinos emitted in β^+ decays. The respective energy losses are taken from Fuller et al. (1982); Pruet & Fuller (2003). ϵ_{cool} is approximated as (Fujimoto et al.

1981)

$$\epsilon_{\text{cool}} = \frac{acT^4}{3\kappa y^2} \quad (2)$$

where the opacity κ is calculated according to Schatz et al. (1999). a is the radiation constant, c the speed of light, and $y = P/g$ the column density. The mass density change $d\rho$ during a time step dt is calculated from P and dT using an equation of state that includes the pressure of the radiation and of a partially degenerate electron gas (Paczynski 1983). The model is coupled to an implicitly solved nuclear reaction network including 688 nuclei from hydrogen to tellurium, which for a given T and ρ calculates dY . We used the same reaction rates as in the multi-zone model.

ONEZONE needs to be coupled with a model predicting the ignition conditions. In the past, a full 1D steady-state hydrogen and helium atmosphere model has been used that evolves the composition as a function of depth during the accretion process until a thermal instability criterion is fulfilled (Cumming & Bildsten 2000). Pressure and composition at that location are then used as initial conditions for ONEZONE. The ignition temperature is not a critical parameter due to the steep temperature rise at the beginning of an X-ray burst. The initial temperature is chosen to be just high enough to initiate a thermonuclear runaway in ONEZONE on a timescale that is sufficiently short to not modify the composition further by any steady state burning. The results for burst timescale, major reaction sequence, and final composition have been shown to agree reasonably well with the first burst calculated with KEPLER (Woosley et al. 2004) and other multi-zone models (Fisker et al. 2008; José et al. 2010). The details of the light curve cannot be predicted accurately, as expected for a one-zone model without radiation transport. As the energy generation and the reaction network are coupled self-consistently, however, ONEZONE can be used to explore the sensitivities of energy generation and the X-ray burst light curve to nuclear reaction rate changes, provided realistic ignition conditions are chosen.

Our goal here is for the single-zone model to most closely resemble a typical burst of the multi-zone model calculation, not the first burst. We therefore extract the ignition conditions for ONEZONE from the baseline calculation of our multi-zone burst model shortly before a typical burst is ignited. The ignition time is defined by significant breakout from the CNO cycle via the $^{15}\text{O}(\alpha,\gamma)$ reaction, and is identified from a peak in the ^{15}O abundance. The ONEZONE model ignition conditions are taken at that time from the zone for which the ONEZONE results for light curve and final composition most closely resemble the multi-zone model results for total luminosity and steady state composition. The chosen ignition conditions were a temperature of 0.386 GK, a pressure of 1.73×10^{22} erg cm $^{-3}$, and hy-

drogen and helium mass fractions of 0.51 and 0.39, respectively.

With these ignition conditions, the peak temperature in ONEZONE agrees with the peak temperature in the hottest zone of the multi-zone model (1.2 GK). Figs. 3 and 4 show that ONEZONE does predict the burst light curve and ashes composition reasonably well. The main difference in the light curve is the sudden drop in luminosity defining the end of the burst in the single-zone model. This is mainly the result of the absence of radiation transport modeling in the one-zone model. As far as the burst ashes are concerned, ONEZONE predicts quite well the main features of the composition, including the $A \approx 40$ peak and subsequent abundance drop, and the main components of the ashes at $A = 56, 60, 64, 68, 72,$ and 76 . The main difference is the additional helium burning in the multi-zone model, which is induced by heating of the ashes in subsequent bursts and is not included in the one-zone approach. Compared to the single-zone results, this helium burning leads to the depletion of helium and other $A < 24$ nuclei, which serve as seeds for α -capture reactions, and the build up of heavier α -chain nuclides at $A = 28$ and 32 . A less important difference is the enhancement in the multi-zone calculation of the only weakly produced mass chains with $A > 60$ owing to the broader range of rp -process freeze out conditions in multiple zones. The ONEZONE reaction flow shown in Fig. 12 is indeed similar to the reaction flow in the multi-zone model during an X-ray bursts (see Fig. 13).

Based on the similarities between ONEZONE and the multi-zone model we expect that reaction rate sensitivities in the αp - and rp -process during a burst can be reasonably well approximated in ONEZONE, with the caveat that lower temperature and density zones contribute to some extent in the multi-zone model. On the other hand, reaction rate sensitivities related to inter-burst burning, for example in the CNO region, and reaction rate sensitivities related to deep helium burning triggered by subsequent bursts, such as sensitivity to α -capture reactions, are not expected to be present in ONEZONE as those burning regimes are not included in the single-zone simulation.

3. RESULTS

In order to quantify the impact of a particular reaction rate variation on X-ray burst model light curve predictions, we define

$$M_{LC}^{(i)} = \int |\langle L_i(t) \rangle - \langle L_0(t) \rangle| dt \quad (3)$$

Here, $\langle L_i(t) \rangle$ is the lightcurve of each variation i , and $\langle L_0(t) \rangle$ is the luminosity of the baseline model. For the multi-zone model $\langle L_i(t) \rangle$ and $\langle L_0(t) \rangle$ are averaged over multiple bursts in the burst sequence. In addition we provide a qualitative classification of the degree of light curve variation caused by the change of a particular reaction rate. Category 1

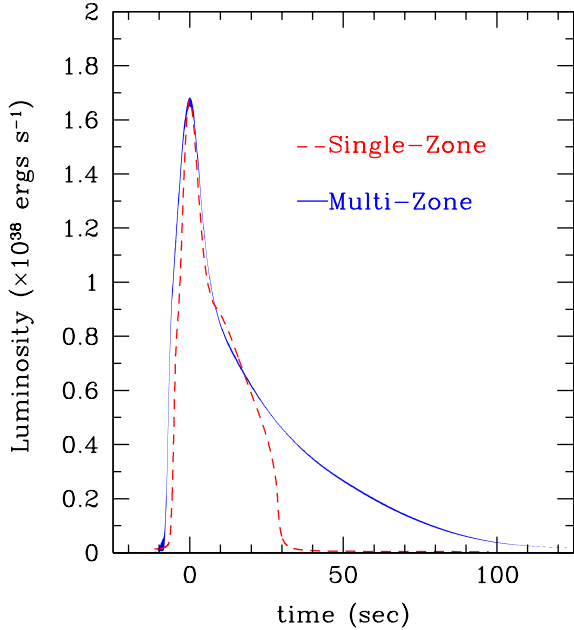


FIG. 4.— X-ray burst light curves predicted by single-zone (red dashed) and multi-zone (blue solid) models. The line width for the multi-zone model light curve indicates the 1σ error of the average light curve.

changes are the largest changes that likely would by themselves affect the interpretation of observational data. Category 2 changes are smaller changes, that may nevertheless be observable given, for example, observational error bars that can be achieved by averaging light curves (Galloway et al. 2004). Category 3 changes are insignificant, but confirm that the varied rate is part of the reaction path and may become significant for larger variations.

The composition of the burst ashes is summed by mass number as electron captures will change the isotopic composition with increasing depth within a constant mass number chain. Summing by mass number allows averaging over a greater depth range as it removes the effects of changes in the composition due to the decay of long-lived radioactive isotopes and weak interactions in the ocean and crust of the neutron star, which are not of interest here.

3.1. Single-zone model results

A total of 1,931 (p, γ), (α ,p), and (α , γ) reactions, together with their respective inverse reactions, were varied individually in the single-zone burst model by factors of 100 up and down. The reactions selected were those at or near the time integrated reaction flow sequence of the baseline single zone model (see Fig. 12).

As expected, the number of individual reaction rate variations that affect the burst light curve significantly (Category 1) is rather small. Fig. 5 and Fig. 6 show the largest resulting variations in the light curve. A large light curve change is produced by variations in 7 (p, γ) reactions, 7 (α ,p) reactions, and the $^{15}\text{O}(\alpha,\gamma)^{19}\text{Ne}$ reaction (see also Tab. 1 and Fig. 12). By far the largest

TABLE 1
REACTIONS THAT IMPACT THE BURST LIGHT CURVE IN THE SINGLE-ZONE X-RAY BURST MODEL.

Rank	Reaction	Type ^a	Sensitivity ^b	Category
1	$^{56}\text{Ni}(\alpha,p)^{59}\text{Cu}$	U	12.5	1
2	$^{59}\text{Cu}(p,\gamma)^{60}\text{Zn}$	D	12.1	1
3	$^{15}\text{O}(\alpha,\gamma)^{19}\text{Ne}$	D	7.9	1
4	$^{30}\text{S}(\alpha,p)^{33}\text{Cl}$	U	7.8	1
5	$^{26}\text{Si}(\alpha,p)^{29}\text{P}$	U	5.3	1
6	$^{61}\text{Ga}(p,\gamma)^{62}\text{Ge}$	D	5.0	1
7	$^{23}\text{Al}(p,\gamma)^{24}\text{Si}$	U	4.8	1
8	$^{27}\text{P}(p,\gamma)^{28}\text{S}$	D	4.4	1
9	$^{63}\text{Ga}(p,\gamma)^{64}\text{Ge}$	D	3.8	1
10	$^{60}\text{Zn}(\alpha,p)^{63}\text{Ga}$	U	3.6	1
11	$^{22}\text{Mg}(\alpha,p)^{25}\text{Al}$	D	3.5	1
12	$^{56}\text{Ni}(p,\gamma)^{57}\text{Cu}$	D	3.4	1
13	$^{29}\text{S}(\alpha,p)^{32}\text{Cl}$	U	2.8	1
14	$^{28}\text{S}(\alpha,p)^{31}\text{Cl}$	U	2.7	1
15	$^{31}\text{Cl}(p,\gamma)^{32}\text{Ar}$	U	2.7	1
16	$^{35}\text{K}(p,\gamma)^{36}\text{Ca}$	U	2.5	2
17	$^{18}\text{Ne}(\alpha,p)^{21}\text{Na}$	D	2.3	2
18	$^{25}\text{Si}(\alpha,p)^{28}\text{P}$	U	1.9	2
19	$^{57}\text{Cu}(p,\gamma)^{58}\text{Zn}$	D	1.7	2
20	$^{34}\text{Ar}(\alpha,p)^{37}\text{K}$	U	1.6	3
21	$^{24}\text{Si}(\alpha,p)^{27}\text{P}$	U	1.4	3
22	$^{22}\text{Mg}(p,\gamma)^{23}\text{Al}$	D	1.1	3
23	$^{65}\text{As}(p,\gamma)^{66}\text{Se}$	U	1.0	3
24	$^{14}\text{O}(\alpha,p)^{17}\text{F}$	U	1.0	3
25	$^{40}\text{Sc}(p,\gamma)^{41}\text{Ti}$	D	0.9	3
26	$^{34}\text{Ar}(p,\gamma)^{35}\text{K}$	D	0.8	3
27	$^{47}\text{Mn}(p,\gamma)^{48}\text{Fe}$	D	0.8	3
28	$^{39}\text{Ca}(p,\gamma)^{40}\text{Sc}$	D	0.8	3

^a Up (U) or down (D) variation that has the largest impact

^b $M_{LC}^{(i)}$ in units of 10^{17}ergs/g/s

change is produced by varying the $^{59}\text{Cu}(p,\gamma)^{60}\text{Zn}$ and $^{59}\text{Cu}(p,\alpha)^{56}\text{Ni}$ rates, because a low $^{59}\text{Cu}(p,\gamma)$ rate or a high $^{59}\text{Cu}(p,\alpha)^{56}\text{Ni}$ rate lead to the formation of a stronger NiCu cycle (van Wormer et al. 1994) that strongly limits synthesis of heavier nuclei. The critical quantity determining the strength of the NiCu cycle is the ratio of the (p, α) to (p, γ) reaction rates at ^{59}Cu . The $^{15}\text{O}(\alpha,\gamma)^{19}\text{Ne}$ reaction rate has a strong impact on the total luminosity and leads to a strongly increased peak energy release when lowered. Variations of 4 additional Category 2 reactions listed in Tab. 1 cause smaller, but still significant changes in the light curve. An additional 9 reactions do have some noticeable impact on the light curve, but rate variations of much more than a factor of 100 will be needed for a significant change. We included the top 28 reactions in the multi-zone variations.

The composition of the burst ashes is affected by a much larger number of reactions. Tab. 4 and Fig. 12 list reactions for which a factor of 100 change (either up or down) of the rate leads to at least a factor of 2 change in the mass fraction of a mass chain with significant ($> 10^{-4}$) mass fraction. The maximum ratio listed in Tab. 4 gives the largest change in the mass fraction of a mass chain, calculated for each mass chain as $\max(X_{\text{initial}}, 10^{-4})/\max(X_{\text{final}}, 10^{-4})$

or, if less than 1, its inverse. Also listed are the mass chains with changes of a factor of 2 or more and 10 or more, respectively. For 21 reactions, changes in the rate by a factor of 100 lead to mass fraction changes in the composition of the burst ashes of a factor of 10 or more (as defined above). For an additional 75 reactions abundance changes range between a factor of 2 and 9. Whereas most reactions affect only a small number of final mass chains in a significant way, typically mass numbers close to the nuclei involved in the reaction, there are a few reactions that affect the final composition broadly. As expected, these tend to be the same reactions that have a significant impact on the burst light curve (see Tab. 1). In some cases, such as $^{15}\text{O}(\alpha,\gamma)^{19}\text{Ne}$, the broad compositional changes induced by a reaction that strongly affects the light curve are less than a factor of 2 and therefore do not appear in Tab. 4.

In total 84 reactions were selected to be explored further in the multi-zone model analysis. This includes all reactions that were found to affect the burst light curve significantly, but only a subset of the reactions that affect the final composition (see reactions marked in Tab. 4 and in Fig. 13).

3.2. Multi-zone model results

The selected 84 reactions were varied individually in the multi-zone model KEPLER, for a total of 168 calculations, each with a full sequence of typically 13-15 bursts. The rate variation factors are listed in Tab. 3. A factor of less than 100 was chosen in cases where the reaction rate uncertainty is likely much smaller. These are mostly reaction rates calculated with the Hauser-Feshbach approach that are closer to stability, where statistical methods should be well applicable (reduction to a factor of 10), (α,p) reactions where limited experimental data hint at a total uncertainty span of a factor of 100 (for example (Parikh et al. 2013; Deibel et al. 2011)), and, in a few cases, reaction rates where some experimental information is available. We do note that with a few exceptions none of the reactions are solely based on direct experimental measurements. The goal was not to determine realistic uncertainties but to err on the side of a larger variation while still minimizing cases where a reaction rate is flagged as important even though it is sufficiently well known. In cases where reaction rates are calculated using shell model information and are dominated by contributions from a few resonances, we calculated upper and lower limits by varying resonance energies by the experimental uncertainty or, when not known experimentally, by 200 keV (see Tab. 3). During this study a compilation of reaction rate uncertainties was published for a small subset of the reactions of interest here (Iliadis et al. 2010). In cases where the new rate uncertainties did not agree within an order of magnitude and, if available, the larger variation showed a significant impact on light curve and composition, we reran the multi-zone model calcu-

lation with a new variation factor estimate based on the data in Iliadis et al. (2010) for a 99.7% confidence range (see Tab. 3). This 3σ confidence range was chosen to be conservative as we want to make sure we are not missing an important sensitivity.

The reaction rate variations that were found to have a significant impact on the burst light curve are listed in order of significance in Tab. 2 and Fig. 13. There are 8 reaction rate variations that affect the light curve strongly (Category 1) (Fig. 7). An additional 11 reaction rate variations lead to smaller but still significant changes (Category 2, see Fig. 8 for examples). We also provide the value for $M_{LC}^{(i)}$ as defined in Eq. 3. Note that while $M_{LC}^{(i)}$ tends to be large for reaction rate variations with a strong impact on the light curve, it does not always provide a reliable quantitative measure for ranking the significance of the light curve impact. $M_{LC}^{(i)}$ weighs changes near peak luminosity more strongly (which may be relevant for some model applications but not for others), and it can become artificially large for small shifts in burst rise or decline, as is for example the case for the $^{17}\text{F}(\alpha,p)^{20}\text{Ne}$ rate variation.

Tab. 5 and Fig. 13 summarize the significant composition changes (at least a factor of 2 change for a mass chain with mass fraction $> 10^{-4}$, see above) induced by the reaction rate variations explored in the multi-zone model. A total of 47 rate variations produce changes of more than a factor of 2 in at least one mass chain, whereas 14 result in changes of a factor of 10 or more. For the multi-zone calculations, changes are defined as the ratio between the up and the down variation. Note that this definition differs from what was used for the single-zone model analysis, where changes were defined relative to a baseline calculation. This addresses ambiguities in the definition of a baseline in the multi-zone model that are a result of our limited burst statistics, combined with rate dependent changes of recurrence time and burst to burst variations. Figs. 9 and 10 show a few examples for composition changes.

The multi-zone model calculations also offer the opportunity to explore the impact of rate changes on the burst recurrence time. Only two reaction variations produce significant changes beyond average burst to burst interval variations, the $^{15}\text{O}(\alpha,\gamma)$ reaction rate variation leads to a 11% change, and the $^{14}\text{O}(\alpha,p)$ reaction rate variation leads to a 7% change. In both cases, only a decrease of the rate has a significant impact and leads to a shortening of the recurrence time (see discussion below).

4. DISCUSSION

The objective of this study is to identify for the one-zone X-ray burst model ONEZONE the important reaction rates that need to be known to predict the burst light curve and composition, and in addition to use that information to identify as many of such reactions as possible in the full 1D multizone X-ray burst model KEPLER.

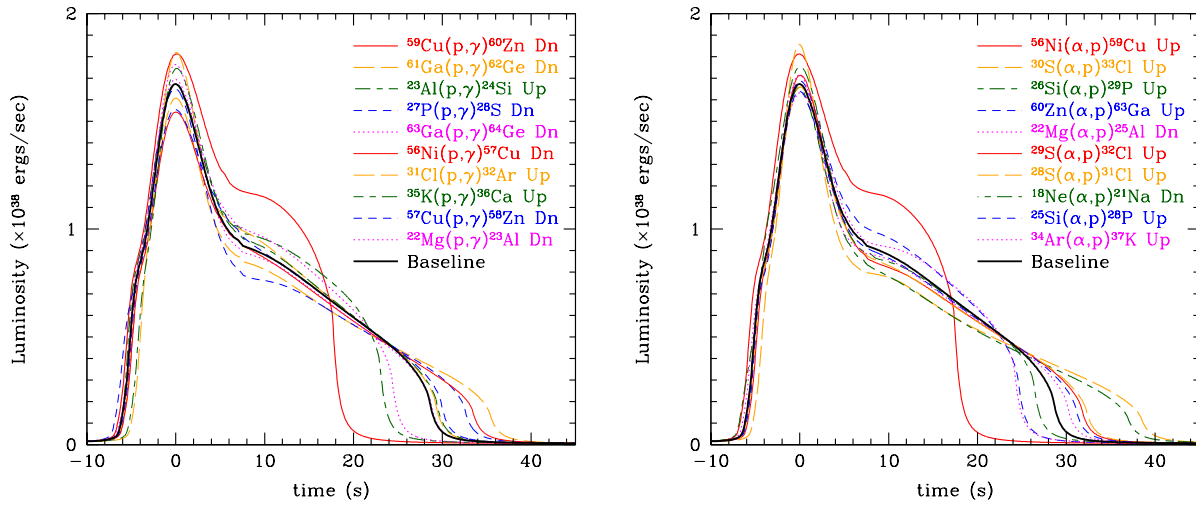


FIG. 5.— The largest changes in single-zone model X-ray burst light curves induced by variations in (p,γ) reaction rates (left panel) and (α,p) reaction rates (right panel). Up denotes a rate increase, Dn a rate decrease. For each rate, only the change with the larger impact is shown.

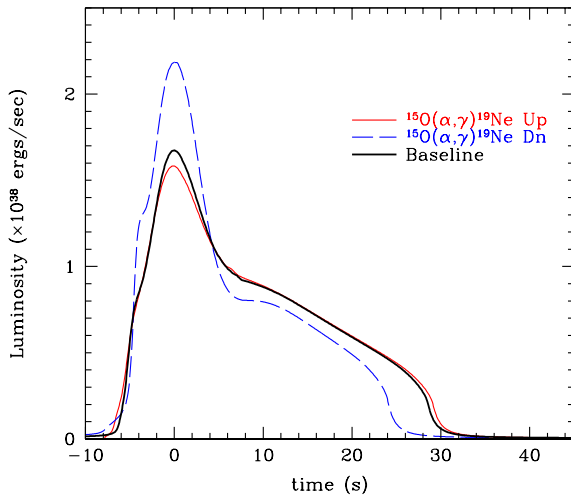


FIG. 6.— Change in single-zone model X-ray burst light curves induced by variation of the $^{15}\text{O}(\alpha,\gamma)$ reaction up (Up) and down (Dn).

4.1. X-ray Light Curves

The reactions that we find to have a significant influence on the burst light curve of the one-zone model are summarized in Fig. 12. The breakout reactions of the hot CNO cycle, $^{15}\text{O}(\alpha,\gamma)$ and $^{18}\text{Ne}(\alpha,p)$ affect the burst light curve onset, which sets the initial conditions for the later stages. $^{14}\text{O}(\alpha,p)$ does not lead to CNO cycle breakout but opens in the early stages of the burst a rapid pathway from ^{14}O to ^{15}O that accelerates the hot CNO cycle.

A second set of reactions that are important for the light curve are the (α,p) reactions in the αp process. In this model they occur on target nuclei ^{22}Mg , $^{24-26}\text{Si}$, $^{28-30}\text{S}$, and ^{34}Ar . As the temperature during the burst rise increases, these nuclei serve as waiting points until it is hot enough for the (α,p) reactions to turn on. In addition, for ^{22}Mg , ^{26}Si , ^{30}S , and ^{34}Ar , a proton capture pathway can

TABLE 2
REACTIONS THAT IMPACT THE BURST LIGHT CURVE
IN THE MULTI ZONE X-RAY BURST MODEL.

Rank	Reaction	Type ^a	Sensitivity ^b	Category
1	$^{15}\text{O}(\alpha,\gamma)^{19}\text{Ne}$	D	16	1
2	$^{56}\text{Ni}(\alpha,p)^{59}\text{Cu}$	U	6.4	1
3	$^{59}\text{Cu}(p,\gamma)^{60}\text{Zn}$	D	5.1	1
4	$^{61}\text{Ga}(p,\gamma)^{62}\text{Ge}$	D	3.7	1
5	$^{22}\text{Mg}(\alpha,p)^{25}\text{Al}$	D	2.3	1
6	$^{14}\text{O}(\alpha,p)^{17}\text{F}$	D	5.8	1
7	$^{23}\text{Al}(p,\gamma)^{24}\text{Si}$	D	4.6	1
8	$^{18}\text{Ne}(\alpha,p)^{21}\text{Na}$	U	1.8	1
9	$^{63}\text{Ga}(p,\gamma)^{64}\text{Ge}$	D	1.4	2
10	$^{19}\text{F}(p,\alpha)^{16}\text{O}$	U	1.3	2
11	$^{12}\text{C}(\alpha,\gamma)^{16}\text{O}$	U	2.1	2
12	$^{26}\text{Si}(\alpha,p)^{29}\text{P}$	U	1.8	2
13	$^{17}\text{F}(\alpha,p)^{20}\text{Ne}$	U	3.5	2
14	$^{24}\text{Mg}(\alpha,\gamma)^{28}\text{Si}$	U	1.2	2
15	$^{57}\text{Cu}(p,\gamma)^{58}\text{Zn}$	D	1.3	2
16	$^{60}\text{Zn}(\alpha,p)^{63}\text{Ga}$	U	1.1	2
17	$^{17}\text{F}(p,\gamma)^{18}\text{Ne}$	U	1.7	2
18	$^{40}\text{Sc}(p,\gamma)^{41}\text{Ti}$	D	1.1	2
19	$^{48}\text{Cr}(p,\gamma)^{49}\text{Mn}$	D	1.2	2

^a Up (U) or down (D) variation that has the largest impact

^b $M_{LC}^{(i)}$ in units of 10^{38}ergs/s

compete with the (α,p) reaction. Therefore, proton capture rates in this pathway become also important. Typically the waiting point is in equilibrium with the following isotone because of the low proton capture Q-value and the strong inverse (γ,p) reaction that enables the much slower (α,p) reaction to compete with the proton capture sequence. In this case, proton capture on the Z + 1 isotone determines the strength of the proton capture branch - for ^{22}Mg , ^{26}Si , ^{30}S , and ^{34}Ar these are the proton captures on ^{23}Al , ^{27}P , ^{31}Cl , and ^{35}K , respectively. In the case of ^{22}Mg and ^{34}Ar the proton capture on the waiting point itself also plays a role, indicating that (p,γ)-(γ,p) equilibrium is not always estab-

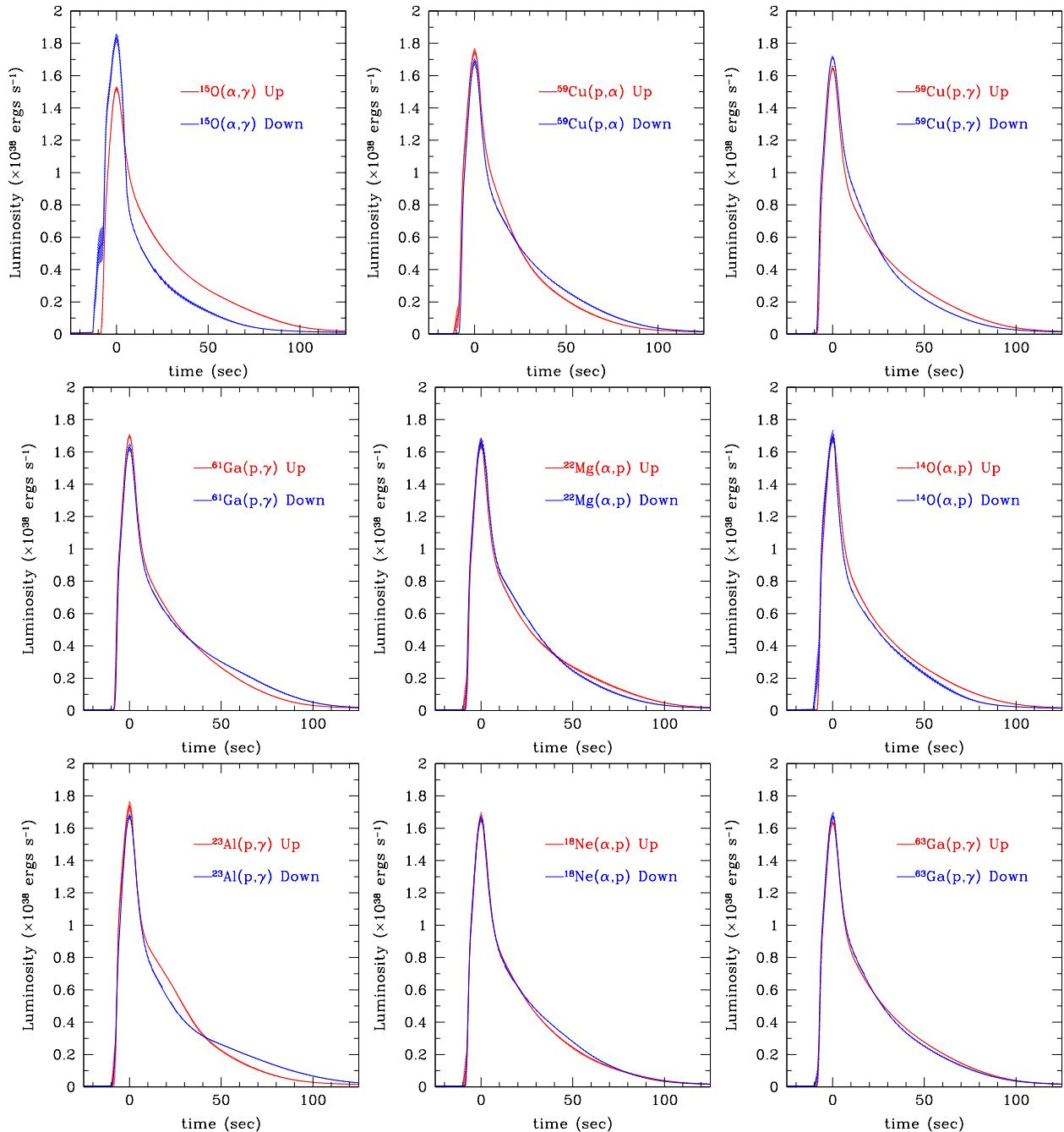


FIG. 7.— The most significant (Category 1, except for $^{63}\text{Ga}(p,\gamma)$) X-ray burst light curve variations in the multi-zone model. Shown is the light curve average over all bursts of the calculated sequence. The line width indicates the 1σ error of the average light curve.

lished.

Also important for the light curve are reactions related to the Ni-Cu and Zn-Ga cycles (van Wormer et al. 1994). Of key importance here is the branching into the cycle at ^{59}Cu and ^{63}Ga , which is determined by the competition of the proton capture rate and the (p,α) rate. Note the (p,α) reactions are listed as (α,p) reactions.

The proton capture rates in the rp -process are

mostly unimportant for determining the burst light curve. This is not surprising, as the process is characterized by proton capture being more rapid than β^+ decays, leaving the β^+ decay rates, which we did not consider in this study, as the critical parameter that determines energy generation. Nevertheless there are exceptions at particular bottle necks. These are either associated with shell structure - ^{39}Ca and ^{56}Ni are isotopes where the rp -process

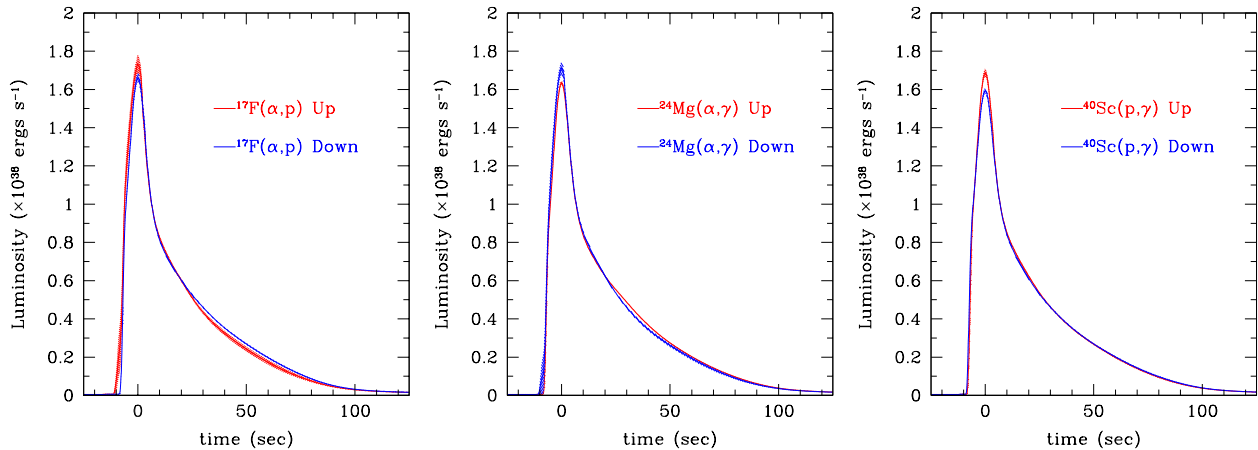


FIG. 8.— Examples for less significant (Category 2) X-ray burst light curve variations in the multi-zone model (see Fig. 7 for details).

crosses the $Z = 20$ and $Z = 28$ proton shells - or with the rp -process waiting points ^{60}Zn and ^{64}Ge , where half-lives are unusually long and proton capture Q -values are low enough to slow down proton captures. As proton capture Q -values tend to be low, (p,γ) - (γ,p) equilibrium tends to play an important role at these waiting points making the proton capture rate on the $Z + 1$ isotones ^{40}Sc , ^{57}Cu , ^{61}Ga , and ^{65}As the important rate. In the case of ^{39}Ca and ^{56}Ni proton capture on the waiting point is also important.

Fig. 13 and Tab. 2 summarize the reactions that have been found to influence the light curve in the multi-zone model. The number of important reactions is somewhat smaller than in the single-zone model, largely because we did use smaller variations in several cases. Additional multi-zone calculations demonstrate that the following reactions would appear in Tab. 2 when varied by the same factor of 100 as the single-zone calculations: $^{22}\text{Mg}(p,\gamma)^{23}\text{Si}$, $^{29}\text{S}(\alpha,p)^{32}\text{Cl}$, $^{30}\text{S}(\alpha,p)^{33}\text{Cl}$, $^{31}\text{Cl}(\alpha,p)^{34}\text{Ar}$ (though with a very small effect), $^{34}\text{Ar}(\alpha,p)^{37}\text{K}$, $^{39}\text{Ca}(p,\gamma)^{40}\text{Sc}$, $^{35}\text{K}(p,\gamma)^{36}\text{Ca}$, and $^{56}\text{Ni}(p,\gamma)^{57}\text{Cu}$. Taking this into account, the qualitative agreement between the single-zone model and the multi-zone model is quite reasonable, validating the overall approach. Nevertheless, the quantitative impact of the various rate variations can be quite different owing to the different conditions in different zones. Only 6 out of the 28 reactions that impact the light curve in the single-zone model have no impact at all in the multi-zone model. 4 of these are (α,p) reactions on the very neutron deficient nuclei ^{24}Si , ^{25}Si , ^{28}S . This may be due to contributions from zones in the multi-zone model, where lower peak temperatures lead to a somewhat less pronounced and less extended αp -process. This may also explain the unimportance of $^{34}\text{Ar}(p,\gamma)^{35}\text{K}$ in the multi-zone model and the fact that in general the (α,p) reactions on heavier nuclei are less important in the multi-zone model than they are in the single-zone model. A detailed analysis of the

origin of the differences between single zone and multi-zone model sensitivities is beyond the scope of this work and would require considerable additional computational effort.

There are also a number of reaction variations that do not impact the light curve in the single-zone model, but have a significant impact on the light curve prediction of the multi-zone model. These reactions fall mostly into two categories: reactions on ^{17}F and ^{19}F that affect the CNO cycles and the helium burning reactions $^{12}\text{C}(\alpha,\gamma)^{16}\text{O}$ and $^{24}\text{Mg}(\alpha,\gamma)^{28}\text{Si}$. The former group likely affects burning between bursts and in shallower zones where the rp -process is mostly absent or less dominant. The latter group affects the helium burning phase once hydrogen is exhausted and in particular the additional helium burning that occurs when a layer of burst ashes is reheated from the ignition of a subsequent burst above it. Both burning regimes are neglected in the single-zone approximation. We were able to identify these reactions in the multi-zone model because we chose to vary them for other reasons than light curve impact in the single-zone model. We cannot exclude the possibility that there are a few additional reactions not listed here that do not appear to be important in the single zone model, but that would affect the multi-zone model predictions, however.

4.2. Composition

Fig. 12 and Tab. 4 summarize the reactions that affect the composition of the burst ashes in the single-zone model significantly (by more than a factor of 2 for mass chains with a mass fraction of more than 10^{-4}). Most reactions along the reaction path affect the composition. An exception are reactions between Ca and Ni, where the rp -process splits into multiple parallel paths. There, only reactions on the path closest to stability are important for the final composition, as this is where the longest β^+ decay half-lives will be located that define the bottle-necks that determine the composition in this mass region.

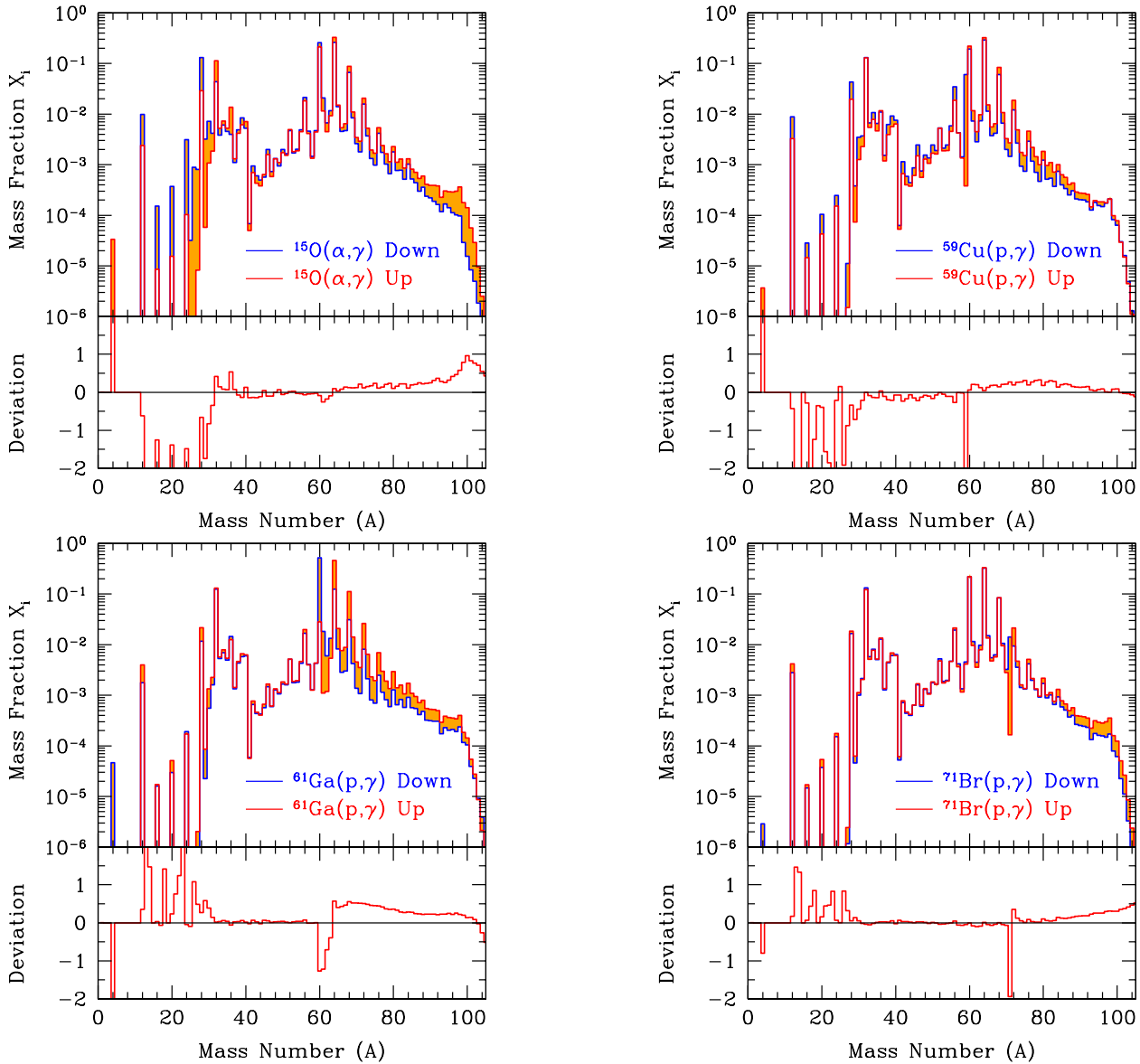


FIG. 9.— Examples for reaction rate variations that affect the composition of the multi-zone model burst ashes in a broad range of mass chains. The lower panel displays the base 10 logarithm of the mass fraction ratio of the up to the down variation.

The most abundant mass chains that dominate the composition of the burst ashes as calculated by the single-zone model (mass fractions $> 10^{-2}$) are $A = 12, 56, 60, 64, 68, 72,$ and 76 . Only a small number of reactions affect these mass chains significantly - these are proton captures on ^{56}Ni , ^{61}Ga , ^{65}Ge , ^{67}As , ^{57}Cu , ^{55}Co , and ^{59}Cu together with the $^{56}\text{Ni}(\alpha, p)$ reaction. An additional 38 reactions affect mass chains with mass fractions $> 10^{-3}$.

It was not feasible to vary all the important reactions identified in the single-zone model in individual multi-zone model runs. Nevertheless, by varying a subset of rates we do find 47 reactions that affect the burst ashes significantly (Fig. 13 and Tab. 5). We also find 37 reactions that do not affect the composition of the ashes significantly and that are also

indicated in Fig. 13. The most important reaction rate uncertainties among the subset of 47 relevant reaction rates will be the ones that affect the most abundant mass chains, and the ones that affect mass chains that are of particular interest because of their impact on ocean and crust physics. The most abundant mass chains in the multi-zone model ($> 10^{-2}$) are $A = 28, 32, 56, 60, 64, 68,$ and 72 . Overall these abundances are quite robust, with no reaction causing a change by more than a factor of 10. The set of reactions affecting the $A = 56, 60, 64, 68,$ and 72 mass chains by more than a factor of 2 is very small. $^{56}\text{Ni}(\alpha, p)^{59}\text{Cu}$ affects $A = 56,$ $^{61}\text{Ga}(\text{p}, \gamma)^{62}\text{Ge}$ has a broad impact on $A = 60, 64,$ and $68,$ and both, $^{69}\text{Se}(\text{p}, \gamma)^{70}\text{Br}$ and $^{71}\text{Br}(\text{p}, \gamma)^{72}\text{Kr}$ affect $A = 72$. The $A = 28$ mass chain is af-

ected by $^{12}\text{C}(\alpha,\gamma)^{16}\text{O}$, $^{15}\text{O}(\alpha,\gamma)^{19}\text{Ne}$, $^{16}\text{O}(\alpha,\text{p})^{19}\text{F}$, $^{18}\text{Ne}(\alpha,\text{p})^{21}\text{Na}$, $^{22}\text{Mg}(\alpha,\text{p})^{25}\text{Al}$, $^{23}\text{Mg}(\alpha,\text{p})^{26}\text{Al}$ and $^{24}\text{Mg}(\alpha,\gamma)^{28}\text{Si}$, whereas $A = 32$ is only affected by $^{15}\text{O}(\alpha,\gamma)^{19}\text{Ne}$. Reactions such as $^{12}\text{C}(\alpha,\gamma)^{16}\text{O}$, $^{16}\text{O}(\alpha,\text{p})^{19}\text{F}$, and $^{24}\text{Mg}(\alpha,\gamma)^{28}\text{S}$ are not expected to occur in the presence of hydrogen, as proton capture rates on these target isotopes are much faster. This indicates late time helium burning as the source of these abundance peaks, which also explains their absence in the single-zone model.

Among the mass chains that affect ocean and crust physics, $A = 12$ stands out. ^{12}C produced by X-ray bursts and reignited deeper in the neutron star ocean is the leading model to explain the occasionally observed superbursts. The small mass fraction of ^{12}C produced in current X-ray burst models (0.4% in our model) is a major issue in this context because super burst models require ^{12}C mass fractions in the 20% range (Cumming et al. 2006) to achieve ignition and explain burst energetics. We find that only four reactions, $^{15}\text{O}(\alpha,\gamma)^{19}\text{Ne}$, $^{56}\text{Ni}(\alpha,\text{p})^{59}\text{Cu}$, $^{59}\text{Cu}(\text{p},\gamma)^{60}\text{Zn}$, and $^{61}\text{Ga}(\text{p},\gamma)^{62}\text{Ge}$ affect ^{12}C production by more than a factor of 2, and none affect it by more than a factor of 10, as would be required to explain the origin of superbursts. With the caveat that we studied only a limited set of reactions, this may indicate that the problem of the small ^{12}C production in X-ray bursts is not caused by nuclear physics uncertainties.

It has recently been found that the presence of nuclei with odd mass numbers may lead to strong crust cooling via electron capture- β -decay Urca cycles (Schatz et al. 2014). The cooling rates are directly proportional to the abundance of the respective mass chain. Reaction rate uncertainties that affect odd mass chains will therefore be of particular importance. The most abundant odd mass chains in the burst ashes are $A = 61, 63, 65$, and 69 , which have mass fractions of close to 10^{-2} or larger. In our subset of reaction rate variations we identify proton captures on ^{61}Zn , ^{61}Ga , ^{63}Ga , ^{65}Ge , ^{66}Ge , ^{67}As , and ^{69}Se as important for determining the amount of these nuclides in the burst ashes.

4.3. Recurrence time

Only three reaction variations were found to significantly (beyond average burst to burst interval variations) affect burst recurrence times: $^{15}\text{O}(\alpha,\gamma)^{19}\text{Ne}$, $^{14}\text{O}(\alpha,\text{p})^{17}\text{F}$, and the 3α reaction. Variation of the 3α reaction rate has a small effect because the rate is relatively well known. A change of the rate of 20% up or down results in a recurrence time change of about 4%. As expected, an increase of the 3α -reaction rate leads to faster burst ignition and a shorter recurrence time, indicating that indeed as predicted the 3α -reaction is the main burst ignition mechanism (Strohmayer & Bildsten 2006). On the other hand, only a decrease of the $^{14}\text{O}(\alpha,\text{p})^{17}\text{F}$ and $^{15}\text{O}(\alpha,\gamma)^{19}\text{Ne}$ reactions has a strong impact, and, somewhat counterintuitively,

leads to faster burst ignition and a decrease in recurrence time by 7% and 11%, respectively.

A possible explanation is the effect of these reactions on the operation of the hot CNO cycle prior to burst ignition (see also the discussion in Fisker et al. 2006). Energy generation by the hot CNO cycle is given by $5.8 \times 10^{15} Z_{\text{CNO}} \text{ ergs g}^{-1} \text{ s}^{-1}$ with Z_{CNO} being the mass fraction of CNO nuclei (Strohmayer & Bildsten 2006). There exists a positive feedback loop between the hot CNO cycle and the 3α reaction. As the hot CNO cycle increases the ^4He abundance, the 3α reaction rate, which depends strongly on the ^4He abundance, will increase. This will increase the amount of CNO nuclei Z in the hot CNO cycle further increasing ^4He production. As the energy generation in the hot CNO cycle increases with Z this may significantly affect burst ignition. The $^{15}\text{O}(\alpha,\gamma)^{19}\text{Ne}$ reaction may then act as a “valve” removing material from the CNO cycle, damping the ^4He abundance feedback loop, slowing down energy generation, and delaying burst ignition. Thus, a smaller $^{15}\text{O}(\alpha,\gamma)^{19}\text{Ne}$ reaction increases energy generation between bursts via the CNO cycle, decreases recurrence times, and for a given accretion rate pushes models closer to the boundary to stable burning. This interpretation is supported by the trends in peak luminosity and burst duration. Fig. 11 shows recurrence time, peak luminosity, and burst timescale τ for additional multi-zone model variations of the $^{15}\text{O}(\alpha,\gamma)^{19}\text{Ne}$ reaction rate. A smaller $^{15}\text{O}(\alpha,\gamma)^{19}\text{Ne}$ reaction rate leads to shorter recurrence times, higher peak brightness, and shorter bursts, just as one would expect for a larger $^4\text{He}/\text{H}$ ratio at burst ignition that would be the result of a stronger CNO cycle in-between bursts. We also confirm previous results (Fisker et al. 2006) that a lower $^{15}\text{O}(\alpha,\gamma)^{19}\text{Ne}$ reaction rate leads to an increase in ^{12}C production (Fig. 11). It has been shown previously that stable burning of hydrogen and helium can lead to the production of large amounts of ^{12}C (Schatz et al. 2003; Stevens et al. 2014). Increased ^{12}C production would therefore be expected for an increase in stable burning between bursts caused by a reduced $^{15}\text{O}(\alpha,\gamma)^{19}\text{Ne}$ reaction rate.

The $^{14}\text{O}(\alpha,\text{p})^{17}\text{F}$ reaction may further support this mechanism by opening a pathway to bypass the ^{14}O β^+ decay in the hot CNO cycle via the $^{14}\text{O}(\alpha,\text{p})^{17}\text{F}(\text{p},\gamma)^{18}\text{Ne}(\beta^+)^{18}\text{F}(\text{p},\alpha)^{15}\text{O}$ reaction sequence. This will increase the ^{15}O abundance relative to the ^{14}O abundance in the hot CNO cycle. An increase of the $^{14}\text{O}(\alpha,\text{p})^{17}\text{F}$ reaction rate will therefore also lead to more efficient breakout of the CNO cycle via $^{15}\text{O}(\alpha,\gamma)^{19}\text{Ne}$.

This effect can only occur if conditions for breakout via $^{15}\text{O}(\alpha,\gamma)$ are reached prior to burst ignition for a long enough time for the hot CNO cycle to operate so that breakout occurs in parallel to the hot CNO cycle. If on the other hand, the time between the onset of the $^{15}\text{O}(\alpha,\gamma)^{19}\text{Ne}$ reaction and ignition

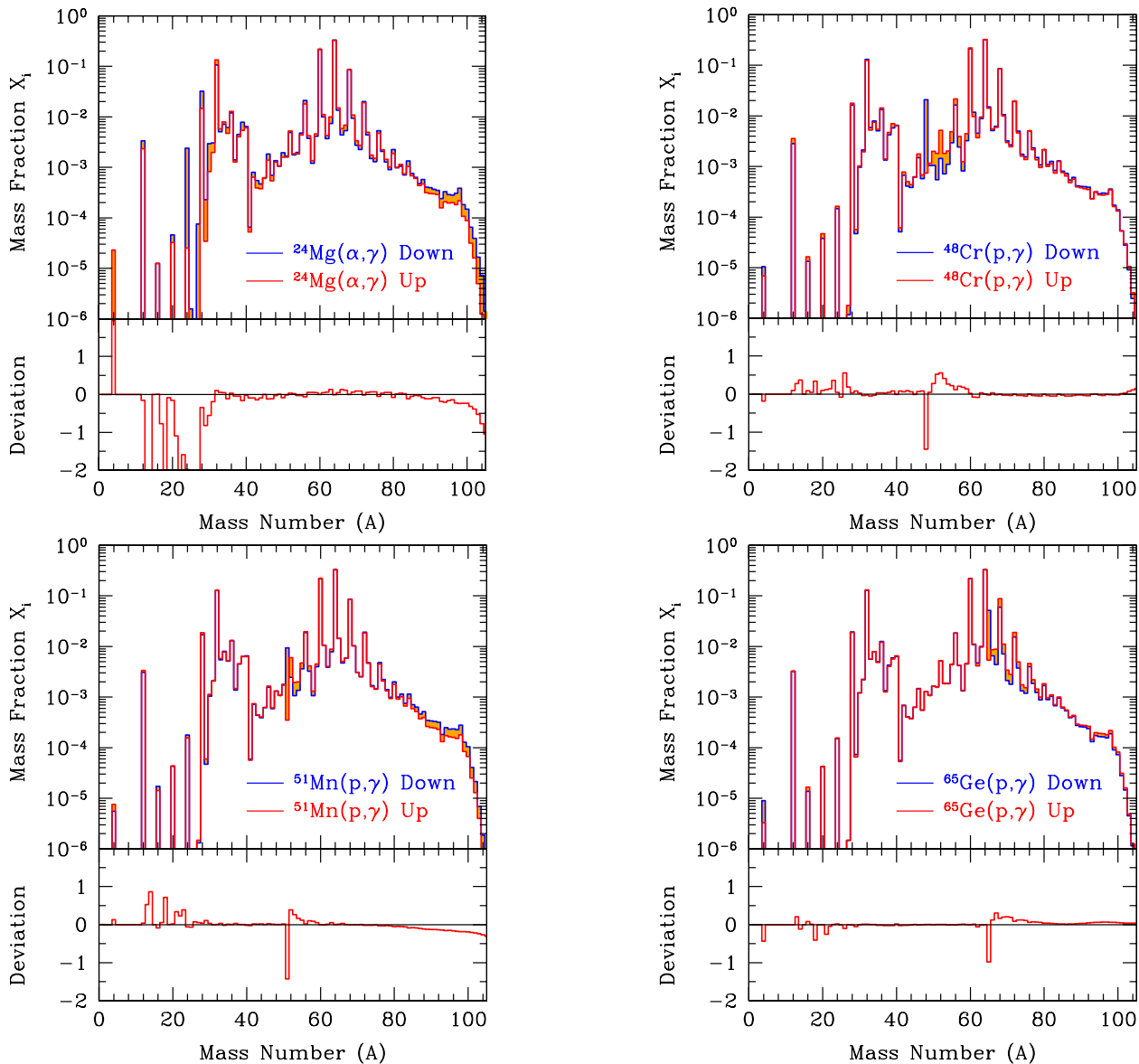


FIG. 10.— Examples for reaction rate variations that affect the composition of the multi-zone model burst ashes in a small number of mass chains. See Fig. 9 for details.

is short, one would expect the opposite behavior, with a larger $^{15}\text{O}(\alpha,\gamma)^{19}\text{Ne}$ reaction leading to ignition sooner. This may explain why different burst models show different sensitivities to $^{15}\text{O}(\alpha,\gamma)^{19}\text{Ne}$ reaction rate variations (see below).

4.4. Comparison with Other Sensitivity Studies

Our results can be compared with previous studies of the sensitivities of X-ray burst models to reaction rate variations. We emphasize that we do not expect the results to be the same for different models (see discussion below). Nevertheless, such a comparison is useful as experimentalists or nuclear theorists may prefer to focus on reaction rates that serve multiple model needs.

Only very few and extremely limited fully self-

consistent one-zone or 1D multi-zone model based sensitivity studies, that take into account the changes in astrophysical conditions induced by rate changes, have been carried out so far, however. Thielemann et al. (2001) varied proton capture rates on ^{27}Si , ^{31}S , ^{35}Ar , and ^{38}Ca and found a strong influence on the burst light curve in their AGILE based 1D multi-zone model. We find that these reactions do not play a significant role in either our single-zone or multi-zone burst model. This agrees with post-processing studies (Iliadis et al. 1999) though the post-processing approach cannot be used to draw firm conclusions (see Section 1). The same multi-zone X-ray burst model has been used by Fisker et al. (2004) to investigate the impact of variations in the $^{30}\text{S}(\alpha,p)^{33}\text{Cl}$ and $^{34}\text{Ar}(\alpha,p)^{37}\text{K}$

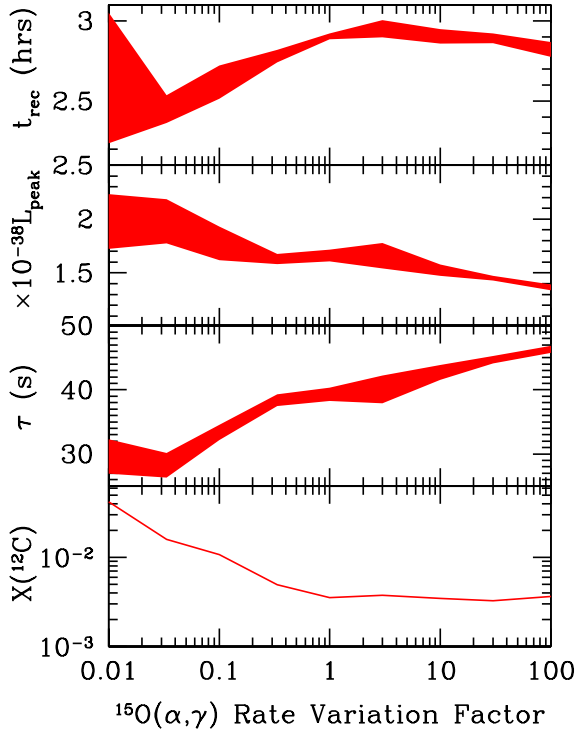


FIG. 11.— Multi-zone model results for burst recurrence time, peak luminosity in erg/s, burst duration, and final ^{12}C mass fraction as functions of the rate multiplier for the $^{15}\text{O}(\alpha,\gamma)^{19}\text{Ne}$ reaction. The band denotes the standard deviation due to burst-to-burst variations.

reaction rates on a double peak structure in their burst light curve. We also find small changes in the burst light curve when these reactions are varied, though the details of the burst shape variations are different. In particular our chosen burst model does not exhibit the double peak structure that Fisker et al. (2004) obtain.

The impact of rate variations of the $^{15}\text{O}(\alpha,\gamma)^{19}\text{Ne}$ reaction has been investigated in a number of multi-zone models (Fisker et al. 2006, 2007; Davids et al. 2011; Keek et al. 2014). Fisker et al. (2007) used the AGILE model and carried out detailed calculations for 8 accretion rates with 9 variations of the $^{15}\text{O}(\alpha,\gamma)^{19}\text{Ne}$ rate each, ranging from a reduction by a factor of 1000 to an increase by a factor of 10 of their recommended rate. They found that for very low $^{15}\text{O}(\alpha,\gamma)^{19}\text{Ne}$ reaction rates burst rise times become longer and longer and eventually burst activity is replaced by an oscillatory burning behavior that resembles a stable burning regime. For an accretion rate and recurrence times that are similar to our study (10% of the Eddington accretion rate and 200 min, respectively) they find that this transition occurs for a rate reduction of a factor of 30 or more. To explore this effect we carried out additional variations of the $^{15}\text{O}(\alpha,\gamma)^{19}\text{Ne}$ rate with our multi-zone model spanning a reaction rate change of /100 to x100. Even for our lowest $^{15}\text{O}(\alpha,\gamma)^{19}\text{Ne}$ rate we do not find the oscillatory behavior found by Fisker et al. (2006). We do find a decrease in

recurrence time (see Fig. 11) with decreasing rate that confirms the effect of the $^{15}\text{O}(\alpha,\gamma)^{19}\text{Ne}$ rate on the hot CNO cycle that Fisker et al. (2006) propose to explain their transition to stable burning, however. Therefore, whereas we confirm that a lower $^{15}\text{O}(\alpha,\gamma)^{19}\text{Ne}$ rate pushes the model towards larger energy generation between bursts and towards stable burning, the effect in our model is not strong enough to actually trigger the transition to stable burning, in contrast to the model of Fisker et al. (2006).

Davids et al. (2011) used the multi-zone X-ray burst code SHIVA to carry out calculations with the same $^{15}\text{O}(\alpha,\gamma)^{19}\text{Ne}$ rate variation used in this work. They find the opposite behavior, with a decreasing $^{15}\text{O}(\alpha,\gamma)^{19}\text{Ne}$ rate leading to longer recurrence times. This may indicate that in their model $^{15}\text{O}(\alpha,\gamma)^{19}\text{Ne}$ does not play a significant role during the hot CNO cycle and rather contributes on short timescales to burst ignition with an additional energy boost. The different behavior is not necessarily surprising as Davids et al. (2011) explore a somewhat different burst regime with longer recurrence times of around 300 min (compared to 175 min and 200 min in this work and Fisker et al. (2006), respectively). In addition, they follow only four bursts and the results may be affected by additional uncertainties from intrinsic burst-to-burst variations.

The only previous large-scale sensitivity study for X-ray bursts was carried out in the post-processing approximation by Parikh et al. (2008). In this approach, a fixed temperature and density profile from a single-zone X-ray burst model is used to calculate energy generation and final composition using a nucleosynthesis network code. As temperature and density are fixed, changes in temperature and density induced by reaction rate changes are neglected. This is a major limitation for X-ray burst studies, where the same reactions that create the burst ashes are the sole source of energy and entirely determine temperature and density evolution. In general, therefore changes in reaction rates in X-ray burst models will lead to changes in temperature and density and associated changes in reaction pathways. Nevertheless post-processing studies are fast and efficient, and can be used to identify qualitatively likely candidates for important reactions by identifying changes in energy generation and composition. It is not generally possible to make reliable predictions of the quantitative impact of a rate change, however. Similarly to our study, Parikh et al. (2008) find that a large number of reactions tend to impact the burst composition. Detailed comparisons are not useful, as Parikh et al. (2008) post processed models with very different temperature and density profiles. They also use a different importance criterion (rates must affect more than three mass chains) than our study. Parikh et al. (2008) do identify a set of 17 reactions that lead to significant changes in energy generation and composition.

Indeed 8 of the 17 reactions have an impact on the burst light curve in either our single-zone or our multi-zone study. These are $^{56}\text{Ni}(\alpha, p)^{59}\text{Cu}$, $^{59}\text{Cu}(p, \gamma)^{60}\text{Zn}$, $^{15}\text{O}(\alpha, \gamma)^{19}\text{Ne}$, $^{23}\text{Al}(p, \gamma)^{24}\text{Si}$, $^{30}\text{S}(\alpha, p)^{33}\text{Cl}$, $^{22}\text{Mg}(\alpha, p)^{25}\text{Al}$, $^{31}\text{Cl}(p, \gamma)^{32}\text{Ar}$, and $^{18}\text{Ne}(\alpha, p)^{21}\text{Na}$. Many rates that we find strongly impact our light curves, however, are not listed in Parikh et al. (2008). Again, this is not surprising as different models are used. For example, we find a strong impact of the $^{14}\text{O}(\alpha, p)^{17}\text{F}$ reaction in our multi-zone model, which is not expected to appear prominently in a single-zone post processing study as it mainly impacts the pre-burst phase and ignition conditions (see Hu et al. (2014) for a post-processing analysis). An example for a rate that we find to be unimportant even though it appears prominently in Parikh et al. (2008) is $^{103}\text{Sn}(\alpha, p)$. The burst model S01 used for post-processing by Parikh et al. (2008) has different astrophysical conditions that lead to a more extended main *rp*-process path that reaches ^{103}Sn , whereas in our model the main *rp*-process ends at lower masses and only a very weak reaction flow reaches the $A = 103$ mass region.

This comparison reinforces an important point. Sensitivity studies by design are specific to a particular model and identify specifically the important nuclear physics in that model. This is of particular importance for X-ray bursts, where a broad range of astrophysical parameters occurs in nature and leads to variations in bursts and nuclear processes. Various models reported in the literature typically choose different astrophysical parameters, that may all be reasonable and reflect different types of systems and sources. Differences among sensitivity studies are therefore expected and reflect the broad needs of nuclear physics data. This is also true for models that use the same input parameters but different astrophysical approximations, for example descriptions for convection or diffusion. The goal of a sensitivity study is to enable the nuclear physics uncertainties of a particular model to be addressed, so that this particular model can be validated against observations. With reliable nuclear physics this validation process can then be used to adjust astrophysical parameters (to effectively extract these from observations) or to guide improvements of the astrophysical approximations.

5. CONCLUSIONS

We present results from the first large-scale investigation of the influence of nuclear reaction rate uncertainties on X-ray burst light curves and ashes that uses a self-consistent multi-zone 1D X-ray burst model. This approach fully accounts for the influence of reaction rate changes on temperature and density conditions, radiation transport, and compositional inertia along a sequence of bursts. The results serve as a road map for nuclear experimental and theoretical work towards reducing nuclear uncertainties in X-ray burst models that describe

bursts in the common mixed hydrogen and helium burning regime.

The most important reaction rate uncertainties identified here are the ones that affect the burst light curve (listed in Tab. 2), the major components of the ashes, ^{12}C production, and the production of odd mass isotopes (Tab. 5). We note that the light curve variations we find from varying a number of single reaction rates with reasonable multiplication factors are comparable or larger than the effects of different surface gravities Zamfir et al. (2012). Clearly reaction rate uncertainties have to be addressed before burst light curve tails can be used to constrain surface gravity and therefore neutron star compactness. We also identified a number of reactions that are not important (Fig. 13).

We also used a one-zone X-ray burst model as closely matched to KEPLER ZM as possible to maximize the number of identified critical reactions with a limited number of multi-zone calculations. For this one-zone model we identified the complete set of important reaction rate uncertainties (Tab. 1, Tab. 4 and Fig. 12). This is the first complete identification of important reaction rates for mixed hydrogen and helium burning bursts in a fully self-consistent one-zone burst model.

We emphasize that our goal was not to calculate realistic uncertainties in a statistical sense, but to flag important reaction rates, and provide one data point on the dependence of observables on this reaction rate. Modifications to the light curve and composition for different variation factors may then be roughly estimated using our results. For a precise analysis calculations would have to be repeated for a particular reaction rate uncertainty, and uncertainty correlations with temperature also had to be included.

More work is needed to quantify the uncertainties of the important reaction rates identified in this work, and to develop targeted approaches to reduce these uncertainties using experiments or nuclear theory. In addition, more sensitivity studies along the lines of this work are needed to arrive at a complete picture of the nuclear physics needs for X-ray burst models. This includes variations of additional reaction rates in the multi-zone burst model investigated here, as the selection based on the single-zone model sensitivity may be incomplete. In addition, sensitivity studies of burst in other burning regimes should be performed.

6. ACKNOWLEDGMENTS

We thank R. Ferguson, M. Klein, S. Warren for help with the data analysis, F.-K. Thielemann for providing the network solver, and L. Bildsten for contributions to the one-zone model. This material is based upon work supported by the National Science Foundation under Grant Numbers PHY-02-016783, PHY-08-22648, and PHY-1430152 (JINA Center for the Evolution of the Elements). AH was supported by an ARC Future Fellowship

(FT120100363) and the US Department of Energy (SC0005012). LK is supported by NASA under award number NNG06EO90A.

REFERENCES

- Angulo, C., Arnould, M., Rayet, M., et al. 1999, *Nucl. Phys. A*, 656, 3
- Buchmann, L. R., & Barnes, C. A. 2006, *Nuclear Physics A*, 777, 254
- Clement, R. R., Bazin, D., Benenson, W., et al. 2004, *Physical Review Letters*, 92, 172502
- Cumming, A., & Bildsten, L. 2000, *ApJ*, 544, 453
- Cumming, A., & Bildsten, L. 2001, *ApJ*, 559, L127
- Cumming, A., Macbeth, J., in 't Zand, J. J. M., & Page, D. 2006, *ApJ*, 646, 429
- Cyburt, R. H., Amthor, A. M., Ferguson, R., et al. 2010, *ApJS*, 189, 240
- Dauids, B., Cyburt, R. H., José, J., & Mythili, S. 2011, *ApJ*, 735, 40
- Deibel, C. M., Rehm, K. E., Figueira, J. M., et al. 2011, *Phys. Rev. C*, 84, 045802
- Fisker, J. L., Görres, J., Wiescher, M., & Dauids, B. 2006, *ApJ*, 650, 332
- Fisker, J. L., Schatz, H., & Thielemann, F.-K. 2008, *ApJSuppl.*, 174, 261
- Fisker, J. L., Tan, W., Görres, J., Wiescher, M., & Cooper, R. L. 2007, *ApJ*, 665, 637
- Fisker, J. L., Thielemann, F.-K., & Wiescher, M. 2004, *ApJ*, 608, L61
- Fujimoto, M. Y., Hanawa, T., & Miyaji, S. 1981, *ApJ*, 247, 267
- Fuller, G. M., Fowler, W. A., & Newman, M. J. 1982, *ApJS*, 48, 279
- Galloway, D., in't Zand, J., Chenevez, J., Keek, L., & Brandt, S. 2010, in *COSPAR Meeting*, Vol. 38, 38th COSPAR Scientific Assembly, 2445
- Galloway, D. K., Cumming, A., Kuulkers, E., et al. 2004, *ApJ*, 601, 466
- Galloway, D. K., Muno, M. P., Hartman, J. M., Psaltis, D., & Chakrabarty, D. 2008, *ApJS*, 179, 360
- Gupta, S., Brown, E. F., Schatz, H., Möller, P., & Kratz, K.-L. 2007, *ApJ*, 662, 1188
- Güver, T., & Özel, F. 2013, *ApJ*, 765, L1
- Haensel, P., & Zdunik, J. L. 2008, *Astr. Astrophys.*, 480, 459
- Heger, A., Cumming, A., Galloway, D. K., & Woosley, S. E. 2007, *ApJ*, 671, L141
- Herwig, F., Austin, S. M., & Lattanzio, J. C. 2006, *Phys. Rev. C*, 73, 025802
- Hu, J., He, J. J., Parikh, A., et al. 2014, *Phys. Rev. C*, 90, 025803
- Iliadis, C., Endt, P., Prantzos, N., & Thompson, W. 1999, *ApJ*, 524, 434
- Iliadis, C., Longland, R., Champagne, A. E., Coc, A., & Fitzgerald, R. 2010, *Nucl. Phys. A*, 841, 31
- José, J., Moreno, F., Parikh, A., & Iliadis, C. 2010, *ApJSuppl.*, 189, 204
- Joss, P. 1977, *Nature*, 270, 310
- Kankainen, A., Novikov, Y. N., Schatz, H., & Weber, C. 2012, *European Physical Journal A*, 48, 50
- Keek, L., Cyburt, R. H., & Heger, A. 2014, *ApJ*, 787, 101
- Keek, L., & Heger, A. 2011, *ApJ*, 743, 189
- Keek, L., & in't Zand, J. J. M. 2008, in *Proceedings of the 7th INTEGRAL Workshop*
- Koike, O., Hashimoto, M., Arai, K., & Wanajo, S. 1999, *A&A*, 342, 464
- Lampe, N., Heger, A., & Galloway, D. K. 2015, *ArXiv e-prints*, arXiv:1512.05769
- Langer, C., Montes, F., Aprahamian, A., et al. 2014, *Physical Review Letters*, 113, 032502
- Lewin, W. H. G., van Paradijs, J., & Taam, R. E. 1993, *Space Sci. Rev.*, 62, 223
- Matic, A., van den Berg, A. M., Harakeh, M. N., et al. 2009, *Phys. Rev. C*, 80, 055804
- Oda, T., Hino, M., Muto, K., Takahara, M., & Sato, K. 1994, *Atomic Data and Nuclear Data Tables*, 56, 231
- Özel, F. 2013, *Reports on Progress in Physics*, 76, 016901
- Paczynski, B. 1983, *ApJ*, 267, 315
- Parikh, A., José, J., Iliadis, C., Moreno, F., & Rauscher, T. 2009, *Phys. Rev. C*, 79, 045802
- Parikh, A., José, J., Moreno, F., & Iliadis, C. 2008, *ApJS*, 178, 110
- Parikh, A., José, J., Sala, G., & Iliadis, C. 2013, *Progress in Particle and Nuclear Physics*, 69, 225
- Pruet, J., & Fuller, G. M. 2003, *ApJS*, 149, 189
- Rauscher, T., & Thielemann, F.-K. 2000, *Atomic Data and Nuclear Data Tables*, 75, 1
- Schatz, H. 2006, *International Journal of Mass Spectrometry*, 251, 293
- Schatz, H., Bildsten, L., Cumming, A., & Ouellette, M. 2003, *Nucl. Phys. A*, 718, 247
- Schatz, H., Bildsten, L., Cumming, A., & Wiescher, M. 1999, *ApJ*, 524, 1014
- Schatz, H., & Rehm, K. E. 2006, *Nucl. Phys. A*, 777, 601
- Schatz, H., Aprahamian, A., Goerres, J., et al. 1998, *Phys. Rep.*, 294, 167
- Schatz, H., Aprahamian, A., Barnard, V., et al. 2001, *Phys. Rev. Lett.*, 86, 3471
- Schatz, H., Gupta, S., Möller, P., et al. 2014, *Nature*, 505, 62
- Steiner, A. W., Lattimer, J. M., & Brown, E. F. 2010, *ApJ*, 722, 33
- Stevens, J., Brown, E. F., Cumming, A., Cyburt, R., & Schatz, H. 2014, *ApJ*, 791, 106
- Strohmayer, T., & Bildsten, L. 2006, In: *Compact stellar X-ray sources*. Edited by Walter Lewin & Michiel van der Klis. Cambridge Astrophysics Series, 113
- Strohmayer, T. E., & Brown, E. F. 2002, *ApJ*, 566, 1045
- Taam, R. E. 1980, *ApJ*, 241, 358
- Thielemann, F.-K., Brachwitz, F., Freiburghaus, C., et al. 2001, *Progress in Particle and Nuclear Physics*, 46, 5
- van Wormer, L., Goerres, J., Iliadis, C., Wiescher, M., & Thielemann, F.-K. 1994, *ApJ*, 432, 326
- Wallace, R. K., & Woosley, S. E. 1981, *ApJSuppl.*, 45, 389
- Weaver, T. A., Zimmerman, G. B., & Woosley, S. E. 1978, *ApJ*, 225, 1021
- Weinberg, N. N., Bildsten, L., & Schatz, H. 2006, *ApJ*, 639, 1018
- Woosley, S., & Taam, R. 1976, *Nature*, 263, 101
- Woosley, S., Heger, A., Cumming, A., et al. 2004, *ApJSuppl.*, 151, 75
- Zamfir, M., Cumming, A., & Galloway, D. K. 2012, *ApJ*, 749, 69

TABLE 3
RATE VARIATIONS IN THE MULTI-ZONE MODEL CALCULATIONS.

Reaction	Variation ^b	Reaction	Variation ^b	Reaction	Variation ^b
3α	x1.2 [2]	$^{12}\text{C}(\alpha,\gamma)^{16}\text{O}$	2.0 [3]	$^{12}\text{C}(\text{p},\gamma)^{13}\text{N}$	1.1 [1]
$^{13}\text{N}(\text{p},\gamma)^{14}\text{O}$	10	$^{14}\text{O}(\alpha,\text{p})^{17}\text{F}$	10	$^{15}\text{O}(\alpha,\gamma)^{19}\text{Ne}$	10
$^{16}\text{O}(\alpha,\gamma)^{20}\text{Ne}$	1.80 [1]	$^{16}\text{O}(\alpha,\text{p})^{19}\text{F}$	10	$^{17}\text{F}(\alpha,\text{p})^{20}\text{Ne}$	10
$^{17}\text{F}(\text{p},\gamma)^{18}\text{Ne}$	6.33 ^d	$^{18}\text{F}(\alpha,\text{p})^{21}\text{Ne}$	100	$^{19}\text{F}(\alpha,\text{p})^{22}\text{Ne}$	10
$^{18}\text{Ne}(\alpha,\text{p})^{21}\text{Na}$	30 [4]	$^{19}\text{Ne}(\alpha,\text{p})^{22}\text{Na}$	10	$^{19}\text{Ne}(\text{p},\gamma)^{20}\text{Na}$	100
$^{20}\text{Ne}(\alpha,\gamma)^{24}\text{Mg}$	1.40 [1]	$^{22}\text{Na}(\alpha,\text{p})^{25}\text{Mg}$	10	$^{22}\text{Na}(\text{p},\gamma)^{23}\text{Mg}$	2 [1]
$^{22}\text{Mg}(\alpha,\text{p})^{25}\text{Al}$	10	$^{23}\text{Mg}(\alpha,\text{p})^{26}\text{Al}$	10	$^{24}\text{Mg}(\alpha,\gamma)^{28}\text{Si}$	10
$^{23}\text{Al}(\text{p},\gamma)^{24}\text{Si}$	30-100 ^a	$^{26}\text{Al}(\alpha,\text{p})^{29}\text{Si}$	10	$^{26}\text{Al}(\text{p},\gamma)^{27}\text{Si}$	2 ^d
$^{24}\text{Si}(\alpha,\text{p})^{27}\text{P}$	10	$^{25}\text{Si}(\alpha,\text{p})^{28}\text{P}$	10	$^{26}\text{Si}(\alpha,\text{p})^{29}\text{P}$	10
$^{27}\text{Si}(\text{p},\gamma)^{28}\text{P}$	3 ^d	$^{27}\text{P}(\text{p},\gamma)^{28}\text{S}$	2-3 ^a	$^{29}\text{P}(\text{p},\gamma)^{30}\text{S}$	10
$^{28}\text{S}(\alpha,\text{p})^{31}\text{Cl}$	10	$^{29}\text{S}(\alpha,\text{p})^{32}\text{Cl}$	10	$^{30}\text{S}(\alpha,\text{p})^{33}\text{Cl}$	10
$^{31}\text{S}(\text{p},\gamma)^{32}\text{Cl}$	6 ^d	$^{31}\text{Cl}(\text{p},\gamma)^{32}\text{Ar}$	2-3 ^a	$^{34}\text{Ar}(\alpha,\text{p})^{37}\text{K}$	10
$^{35}\text{Ar}(\text{p},\gamma)^{36}\text{K}$	100	$^{35}\text{K}(\text{p},\gamma)^{36}\text{Ca}$	3-10 ^a	$^{36}\text{K}(\text{p},\gamma)^{37}\text{Ca}$	10
$^{39}\text{Ca}(\text{p},\gamma)^{40}\text{Sc}$	3 ^d	$^{40}\text{Ca}(\text{p},\gamma)^{41}\text{Sc}$	1.40 ^d	$^{40}\text{Sc}(\text{p},\gamma)^{41}\text{Ti}$	100
$^{45}\text{V}(\text{p},\gamma)^{46}\text{Cr}$	100	$^{47}\text{Cr}(\text{p},\gamma)^{48}\text{Mn}$	10	$^{48}\text{Cr}(\text{p},\gamma)^{49}\text{Mn}$	100
$^{49}\text{Cr}(\text{p},\gamma)^{50}\text{Mn}$	10	$^{47}\text{Mn}(\text{p},\gamma)^{48}\text{Fe}$	100	$^{51}\text{Mn}(\text{p},\gamma)^{52}\text{Fe}$	100
$^{52}\text{Fe}(\text{p},\gamma)^{53}\text{Co}$	100	$^{53}\text{Fe}(\text{p},\gamma)^{54}\text{Co}$	100	$^{54}\text{Fe}(\text{p},\gamma)^{55}\text{Co}$	10
$^{54}\text{Co}(\text{p},\gamma)^{55}\text{Ni}$	10	$^{56}\text{Ni}(\alpha,\text{p})^{59}\text{Cu}$	100	$^{56}\text{Ni}(\text{p},\gamma)^{57}\text{Cu}$	5 ^a
$^{57}\text{Cu}(\text{p},\gamma)^{58}\text{Zn}$	100 ^c	$^{59}\text{Cu}(\text{p},\gamma)^{60}\text{Zn}$	100	$^{60}\text{Cu}(\text{p},\gamma)^{61}\text{Zn}$	10
$^{60}\text{Zn}(\alpha,\text{p})^{63}\text{Ga}$	100	$^{61}\text{Zn}(\text{p},\gamma)^{62}\text{Ga}$	100	$^{62}\text{Zn}(\text{p},\gamma)^{63}\text{Ga}$	10
$^{61}\text{Ga}(\text{p},\gamma)^{62}\text{Ge}$	100	$^{63}\text{Ga}(\text{p},\gamma)^{64}\text{Ge}$	10	$^{61}\text{Ge}(\text{p},\gamma)^{62}\text{As}$	100
$^{65}\text{Ge}(\text{p},\gamma)^{66}\text{As}$	100	$^{66}\text{Ge}(\text{p},\gamma)^{67}\text{As}$	100	$^{65}\text{As}(\text{p},\gamma)^{66}\text{Se}$	100
$^{67}\text{As}(\text{p},\gamma)^{68}\text{Se}$	100	$^{69}\text{Se}(\text{p},\gamma)^{70}\text{Br}$	100	$^{70}\text{Br}(\text{p},\gamma)^{71}\text{Kr}$	100
$^{71}\text{Br}(\text{p},\gamma)^{72}\text{Kr}$	100	$^{72}\text{Br}(\text{p},\gamma)^{73}\text{Kr}$	10	$^{73}\text{Kr}(\text{p},\gamma)^{74}\text{Rb}$	10
$^{74}\text{Rb}(\text{p},\gamma)^{75}\text{Sr}$	10	$^{75}\text{Rb}(\text{p},\gamma)^{76}\text{Sr}$	100	$^{76}\text{Rb}(\text{p},\gamma)^{77}\text{Sr}$	10
$^{79}\text{Y}(\text{p},\gamma)^{80}\text{Zr}$	10	$^{83}\text{Zr}(\text{p},\gamma)^{84}\text{Nb}$	10	$^{83}\text{Nb}(\text{p},\gamma)^{84}\text{Mo}$	10
$^{84}\text{Nb}(\text{p},\gamma)^{85}\text{Mo}$	10	$^{85}\text{Mo}(\text{p},\gamma)^{86}\text{Tc}$	100	$^{86}\text{Mo}(\text{p},\gamma)^{87}\text{Tc}$	100
$^{89}\text{Tc}(\text{p},\gamma)^{90}\text{Ru}$	10	$^{92}\text{Rh}(\text{p},\gamma)^{93}\text{Pd}$	10	$^{93}\text{Pd}(\text{p},\gamma)^{94}\text{Ag}$	10

REFERENCES. — [1] Angulo et al. (1999), [2] Herwig et al. (2006), [3] Buchmann & Barnes (2006), [4] Matic et al. (2009)

^a Values approximate. Variation calculated using resonance uncertainty (see text) and depends on temperature.

^b Reaction rates were each multiplied and divided by the factor given. References refer to work that was used in the estimate of the variation factor.

^c Recent experiment reduced uncertainty significantly (Langer et al. 2014)

^d Adjusted with data from Iliadis et al. (2010)

TABLE 4
 REACTIONS THAT IMPACT THE COMPOSITION IN THE SINGLE ZONE X-RAY BURST
 MODEL.

Count	Reaction	Max. Ratio ^a	Affected Mass Numbers with Mass Fraction $> 10^{-4}$	
			max	$> \times 10$ change
1	$^{12}\text{C}(p,\gamma)^{13}\text{N}$	6	16	16
2	$^{15}\text{O}(\alpha,\gamma)^{19}\text{Ne}^*$	4	15	15
3	$^{16}\text{O}(\alpha,\gamma)^{20}\text{Ne}^*$	7	16	16,20-21
4	$^{17}\text{F}(\alpha,p)^{20}\text{Ne}^*$	2	21	21
5	$^{17}\text{F}(p,\gamma)^{18}\text{Ne}^*$	3	19	18-19,21
6	$^{18}\text{F}(\alpha,p)^{21}\text{Ne}^*$	2	23	18,21,23
7	$^{18}\text{Ne}(\alpha,p)^{21}\text{Na}^*$	7	19	18-19,21,24,57
8	$^{20}\text{Ne}(\alpha,\gamma)^{24}\text{Mg}^*$	6	20	20,24
9	$^{22}\text{Na}(\alpha,p)^{25}\text{Mg}^*$	4	27	16,21,25,27
10	$^{22}\text{Na}(p,\gamma)^{23}\text{Mg}^*$	4	23	23
11	$^{22}\text{Mg}(\alpha,p)^{25}\text{Al}^*$	20	22	22
12	$^{23}\text{Mg}(p,\gamma)^{24}\text{Al}$	2	23	23
13	$^{23}\text{Al}(p,\gamma)^{24}\text{Si}^*$	4	57	16,19,21,24,26-28,46,57,70,74,81-82
14	$^{24}\text{Al}(p,\gamma)^{25}\text{Si}$	2	24	24
15	$^{26}\text{Al}(p,\gamma)^{27}\text{Si}^*$	6	27	27
16	$^{26}\text{Si}(\alpha,p)^{29}\text{P}^*$	3	18	18-21,46,57,70,73-75,78,82,86
17	$^{27}\text{Si}(p,\gamma)^{28}\text{P}^*$	3	27	27
18	$^{28}\text{Si}(p,\gamma)^{29}\text{P}$	2	28	28
19	$^{27}\text{P}(p,\gamma)^{28}\text{S}^*$	2	26	26
20	$^{28}\text{P}(p,\gamma)^{29}\text{S}$	2	28	28
21	$^{29}\text{P}(p,\gamma)^{30}\text{S}^*$	4	29	29
22	$^{30}\text{P}(p,\gamma)^{31}\text{S}$	3	31	31
23	$^{28}\text{S}(\alpha,p)^{31}\text{Cl}^*$	2	19	18-19
24	$^{30}\text{S}(\alpha,p)^{33}\text{Cl}^*$	3	18	18-21,46,57,70-71,73-75,77-78,81-83,86
25	$^{31}\text{S}(p,\gamma)^{32}\text{Cl}^*$	6	31	31,33
26	$^{32}\text{Cl}(p,\gamma)^{33}\text{Ar}$	5	32	32-33
27	$^{33}\text{Cl}(p,\gamma)^{34}\text{Ar}$	4	33	33
28	$^{35}\text{Ar}(p,\gamma)^{36}\text{K}^*$	7	35	35-37
29	$^{36}\text{Ar}(p,\gamma)^{37}\text{K}$	4	36	36
30	$^{36}\text{K}(p,\gamma)^{37}\text{Ca}^*$	5	36	36
31	$^{37}\text{K}(p,\gamma)^{38}\text{Ca}$	6	37	37
32	$^{39}\text{K}(p,\gamma)^{40}\text{Ca}$	3	40	40
33	$^{40}\text{Ca}(p,\gamma)^{41}\text{Sc}^*$	6	40	40,42-46
34	$^{41}\text{Sc}(p,\gamma)^{42}\text{Ti}$	10	41	41
35	$^{42}\text{Sc}(p,\gamma)^{43}\text{Ti}$	3	42	42-43
36	$^{43}\text{Ti}(p,\gamma)^{44}\text{V}$	8	43	43-45
37	$^{44}\text{Ti}(p,\gamma)^{45}\text{V}$	2	44	44
38	$^{44}\text{V}(p,\gamma)^{45}\text{Cr}$	7	44	44-45
39	$^{45}\text{V}(p,\gamma)^{46}\text{Cr}^*$	6	45	45-46
40	$^{46}\text{V}(p,\gamma)^{47}\text{Cr}$	2	46	46
41	$^{47}\text{Cr}(p,\gamma)^{48}\text{Mn}^*$	8	47	47
42	$^{48}\text{Cr}(p,\gamma)^{49}\text{Mn}^*$	3	48	48
43	$^{48}\text{Mn}(p,\gamma)^{49}\text{Fe}$	10	48	48
44	$^{49}\text{Mn}(p,\gamma)^{50}\text{Fe}$	7	49	49
45	$^{50}\text{Mn}(p,\gamma)^{51}\text{Fe}$	3	50	50-51
46	$^{51}\text{Mn}(p,\gamma)^{52}\text{Fe}^*$	2	51	51
47	$^{51}\text{Fe}(p,\gamma)^{52}\text{Co}$	5	51	51
48	$^{52}\text{Fe}(p,\gamma)^{53}\text{Co}^*$	7	52	52
49	$^{53}\text{Fe}(p,\gamma)^{54}\text{Co}^*$	3	53	53
50	$^{54}\text{Fe}(p,\gamma)^{55}\text{Co}^*$	3	54	54
51	$^{52}\text{Co}(p,\gamma)^{53}\text{Ni}$	5	52	52
52	$^{53}\text{Co}(p,\gamma)^{54}\text{Ni}$	10	53	53
53	$^{54}\text{Co}(p,\gamma)^{55}\text{Ni}^*$	10	54	54
54	$^{55}\text{Co}(p,\gamma)^{56}\text{Ni}^*$	10	55	55
55	$^{56}\text{Ni}(\alpha,p)^{59}\text{Cu}^*$	7	24	12,16,21-22,24-34,36-39,42,44,46,50,52,54-57,61,63,65-67,69-71,73-75,77-78,80-85
56	$^{56}\text{Ni}(p,\gamma)^{57}\text{Cu}^*$	10	56	56
57	$^{57}\text{Ni}(p,\gamma)^{58}\text{Cu}$	5	57	18-19,21,57-59
58	$^{57}\text{Cu}(p,\gamma)^{58}\text{Zn}^*$	6	57	57
59	$^{58}\text{Cu}(p,\gamma)^{59}\text{Zn}$	30	58	56-58
60	$^{59}\text{Cu}(p,\gamma)^{60}\text{Zn}^*$	10	59	58
61	$^{60}\text{Cu}(p,\gamma)^{61}\text{Zn}^*$	3	61	59
62	$^{60}\text{Zn}(\alpha,p)^{63}\text{Ga}^*$	2	57	12,16,21-22,24-34,36-39,42,44,46,50,52,54-57,61,65-67,69-71,73-75,77-78,80-85
63	$^{61}\text{Zn}(p,\gamma)^{62}\text{Ga}^*$	10	61	61
64	$^{62}\text{Zn}(p,\gamma)^{63}\text{Ga}^*$	5	62	61,63
				21,24,27,57
				63
				62

TABLE 4 — *Continued*

Count	Reaction	Max. Ratio ^a	Affected Mass Numbers with Mass Fraction $> 10^{-4}$		
			max	$> \times 10$ change	$\times 2 < \text{change} < \times 10$
65	$^{61}\text{Ga}(p,\gamma)^{62}\text{Ge}^*$	8	60		12,18-19,60-68
66	$^{63}\text{Ga}(p,\gamma)^{64}\text{Ge}^*$	10	63	63	21,24,27,57
67	$^{64}\text{Ga}(p,\gamma)^{65}\text{Ge}$	6	65		65-67
68	$^{65}\text{Ge}(p,\gamma)^{66}\text{As}^*$	30	65	65	66-67
69	$^{66}\text{Ge}(p,\gamma)^{67}\text{As}^*$	20	66	66	67
70	$^{66}\text{As}(p,\gamma)^{67}\text{Se}$	5	66		66
71	$^{67}\text{As}(p,\gamma)^{68}\text{Se}^*$	30	67	67	
72	$^{68}\text{As}(p,\gamma)^{69}\text{Se}$	5	69		69-71
73	$^{69}\text{Se}(p,\gamma)^{70}\text{Br}^*$	20	69	69	70-71
74	$^{70}\text{Se}(p,\gamma)^{71}\text{Br}$	10	70	70	71
75	$^{70}\text{Br}(p,\gamma)^{71}\text{Kr}^*$	3	70		70
76	$^{71}\text{Br}(p,\gamma)^{72}\text{Kr}^*$	10	71	71	
77	$^{72}\text{Br}(p,\gamma)^{73}\text{Kr}^*$	5	73		73-75
78	$^{73}\text{Kr}(p,\gamma)^{74}\text{Rb}^*$	20	73	73	74-78
79	$^{74}\text{Kr}(p,\gamma)^{75}\text{Rb}$	10	74	74	75
80	$^{74}\text{Rb}(p,\gamma)^{75}\text{Sr}^*$	3	74		74
81	$^{75}\text{Rb}(p,\gamma)^{76}\text{Sr}^*$	9	75		75-76
82	$^{76}\text{Rb}(p,\gamma)^{77}\text{Sr}^*$	5	77		77-78
83	$^{77}\text{Sr}(p,\gamma)^{78}\text{Y}$	10	77	77	
84	$^{78}\text{Sr}(p,\gamma)^{79}\text{Y}$	6	78		78,80-85
85	$^{78}\text{Y}(p,\gamma)^{79}\text{Zr}$	10	80	80	78-79,81-92
86	$^{79}\text{Y}(p,\gamma)^{80}\text{Zr}^*$	5	80		80
87	$^{80}\text{Y}(p,\gamma)^{81}\text{Zr}$	5	81		81-85
88	$^{81}\text{Zr}(p,\gamma)^{82}\text{Nb}$	5	81		81
89	$^{82}\text{Zr}(p,\gamma)^{83}\text{Nb}$	3	82		82-85
90	$^{82}\text{Nb}(p,\gamma)^{83}\text{Mo}$	2	82		82
91	$^{83}\text{Nb}(p,\gamma)^{84}\text{Mo}^*$	3	84		83-84
92	$^{84}\text{Nb}(p,\gamma)^{85}\text{Mo}^*$	3	85		84-85
93	$^{85}\text{Nb}(p,\gamma)^{86}\text{Mo}$	2	85		85
94	$^{85}\text{Mo}(p,\gamma)^{86}\text{Tc}^*$	3	85		85
95	$^{86}\text{Mo}(p,\gamma)^{87}\text{Tc}^*$	3	86		86
96	$^{88}\text{Tc}(p,\gamma)^{89}\text{Ru}$	4	88		88

* Reaction also varied in multi-zone model.

^a Abundance ratio relative to the baseline calculation

TABLE 5
 REACTIONS THAT IMPACT THE COMPOSITION IN THE MULTI-ZONE X-RAY BURST
 MODEL.

Count	Reaction	Max. Ratio ^a	Affected Mass Numbers with Mass Fraction $> 10^{-4}$		
			max	$> \times 10$ change	$\times 2 < \text{change} < \times 10$
1	${}^8\text{Be}(\alpha,\gamma){}^{12}\text{C}$	3	98		30,93-99
2	${}^{12}\text{C}(\alpha,\gamma){}^{16}\text{O}$	2	28		28
3	${}^{14}\text{O}(\alpha,p){}^{17}\text{F}$	4	29		29
4	${}^{15}\text{O}(\alpha,\gamma){}^{19}\text{Ne}$	30	29	24,29	12,20,26-28,30-32,36,91-92,95-98
5	${}^{16}\text{O}(\alpha,p){}^{19}\text{F}$	3	28		28
6	${}^{17}\text{F}(\alpha,p){}^{20}\text{Ne}$	3	98		90,93-99
7	${}^{18}\text{Ne}(\alpha,p){}^{21}\text{Na}$	4	30		28,30,98-99
8	${}^{22}\text{Mg}(\alpha,p){}^{25}\text{Al}$	4	30		28-30
9	${}^{23}\text{Mg}(\alpha,p){}^{26}\text{Al}$	2	28		28
10	${}^{24}\text{Mg}(\alpha,\gamma){}^{28}\text{Si}$	20	24	24	28-30
11	${}^{23}\text{Al}(p,\gamma){}^{24}\text{Si}$	2	75		75,79
12	${}^{26}\text{Al}(\alpha,p){}^{29}\text{Si}$	4	26		26,29
13	${}^{29}\text{P}(p,\gamma){}^{30}\text{S}$	3	98		90,92-99
14	${}^{40}\text{Sc}(p,\gamma){}^{41}\text{Ti}$	3	29		29
15	${}^{45}\text{V}(p,\gamma){}^{46}\text{Cr}$	10	45	45	46
16	${}^{47}\text{Cr}(p,\gamma){}^{48}\text{Mn}$	2	47		47
17	${}^{48}\text{Cr}(p,\gamma){}^{49}\text{Mn}$	30	48	48	51-53
18	${}^{49}\text{Cr}(p,\gamma){}^{50}\text{Mn}$	5	49		49
19	${}^{47}\text{Mn}(p,\gamma){}^{48}\text{Fe}$	2	98		97-99
20	${}^{51}\text{Mn}(p,\gamma){}^{52}\text{Fe}$	30	51	51	52
21	${}^{52}\text{Fe}(p,\gamma){}^{53}\text{Co}$	40	52	52	53-55,57
22	${}^{53}\text{Fe}(p,\gamma){}^{54}\text{Co}$	40	53	53	57-58
23	${}^{54}\text{Fe}(p,\gamma){}^{55}\text{Co}$	6	54		54
24	${}^{56}\text{Ni}(\alpha,p){}^{59}\text{Cu}$	5	29		12,29-30,56,75,78-79,82
25	${}^{59}\text{Cu}(p,\gamma){}^{60}\text{Zn}$	200	59	59	12,29-30,75,78-79
26	${}^{60}\text{Cu}(p,\gamma){}^{61}\text{Zn}$	2	98		93-98
27	${}^{60}\text{Zn}(\alpha,p){}^{63}\text{Ga}$	2	98		97-98
28	${}^{61}\text{Zn}(p,\gamma){}^{62}\text{Ga}$	9	61		61-63
29	${}^{62}\text{Zn}(p,\gamma){}^{63}\text{Ga}$	7	62		62,90-99
30	${}^{61}\text{Ga}(p,\gamma){}^{62}\text{Ge}$	20	60	60-61	12,30,62-81
31	${}^{63}\text{Ga}(p,\gamma){}^{64}\text{Ge}$	3	63		63
32	${}^{65}\text{Ge}(p,\gamma){}^{66}\text{As}$	10	65	65	67
33	${}^{66}\text{Ge}(p,\gamma){}^{67}\text{As}$	20	66	66	67
34	${}^{67}\text{As}(p,\gamma){}^{68}\text{Se}$	100	67	67	93-95,97-98
35	${}^{69}\text{Se}(p,\gamma){}^{70}\text{Br}$	7	69		69,71-75
36	${}^{71}\text{Br}(p,\gamma){}^{72}\text{Kr}$	90	71	71	72,98
37	${}^{72}\text{Br}(p,\gamma){}^{73}\text{Kr}$	2	98		74,93-94,96-98
38	${}^{73}\text{Kr}(p,\gamma){}^{74}\text{Rb}$	4	73		73,75
39	${}^{75}\text{Rb}(p,\gamma){}^{76}\text{Sr}$	40	75	75	
40	${}^{79}\text{Y}(p,\gamma){}^{80}\text{Zr}$	6	79		79
41	${}^{83}\text{Zr}(p,\gamma){}^{84}\text{Nb}$	3	83		83
42	${}^{83}\text{Nb}(p,\gamma){}^{84}\text{Mo}$	2	83		83
43	${}^{84}\text{Nb}(p,\gamma){}^{85}\text{Mo}$	3	84		84
44	${}^{85}\text{Mo}(p,\gamma){}^{86}\text{Tc}$	3	85		85,90-98
45	${}^{86}\text{Mo}(p,\gamma){}^{87}\text{Tc}$	7	86		86,90-92
46	${}^{89}\text{Tc}(p,\gamma){}^{90}\text{Ru}$	3	89		89
47	${}^{92}\text{Rh}(p,\gamma){}^{93}\text{Pd}$	3	98		91,93-98

^a Abundance ratio between up and down variations of the reaction rate

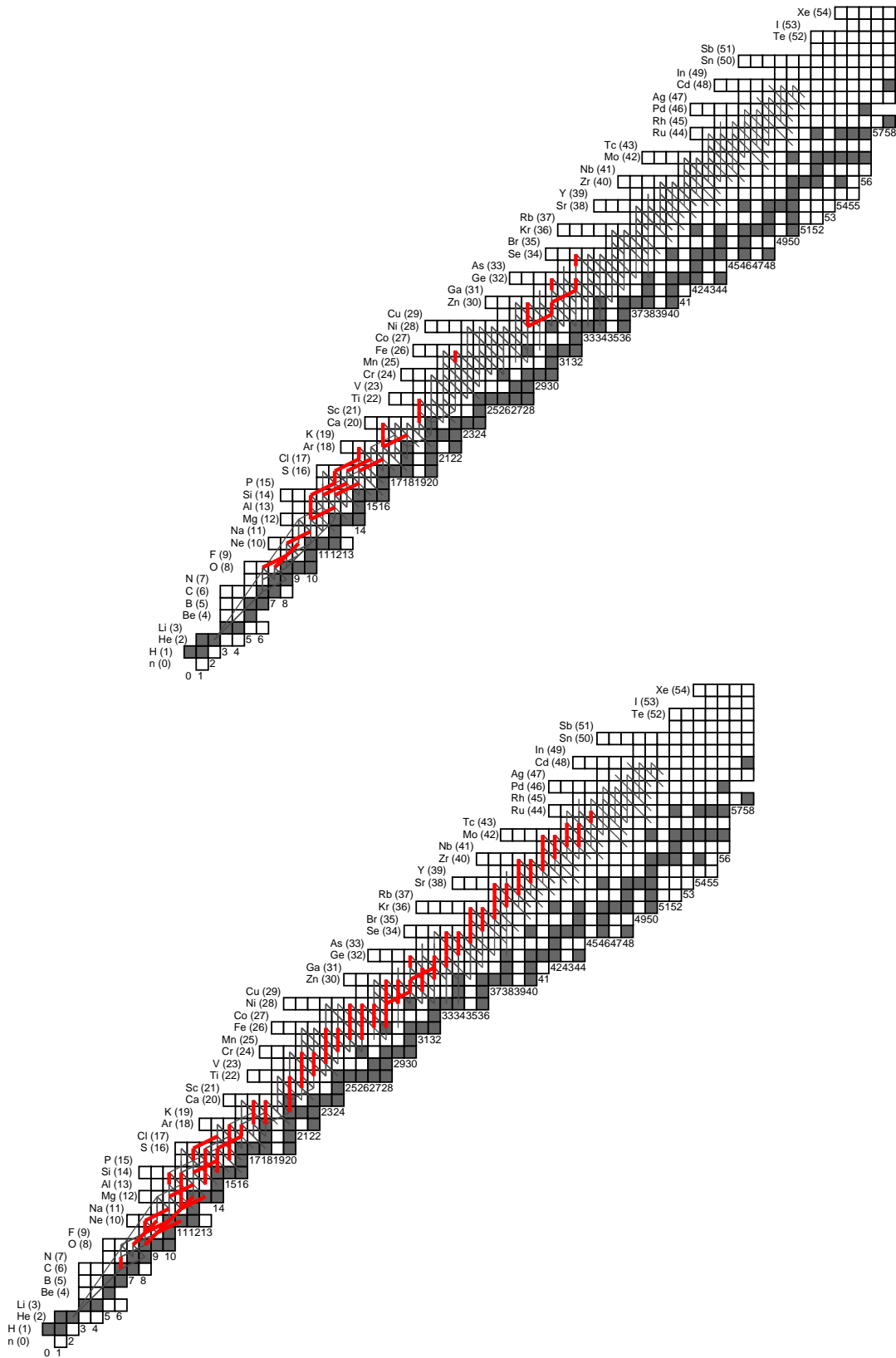


FIG. 12.— Time integrated net reaction flows in the single-zone model (black). Thick red lines indicate reactions that significantly affect the light curve (upper panel) and composition of the burst ashes (lower panel). Note that proton capture flows carry large uncertainties because they are determined from the difference between proton capture and the inverse photodisintegration flows, which both can be very large.

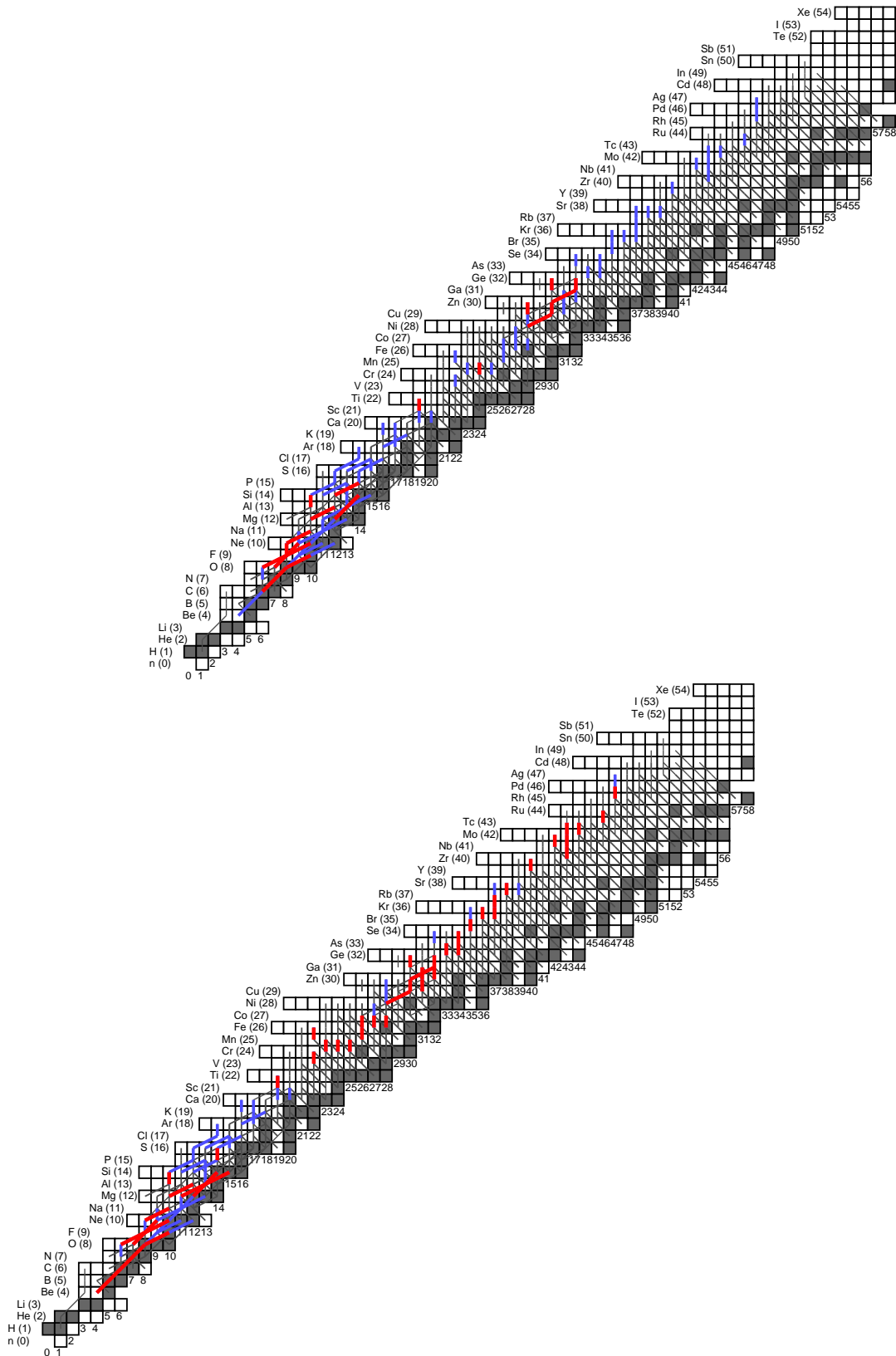


FIG. 13.— Time integrated net reaction flows in the multi-zone model (black). Flows are a weighted average over all zones. Thick red lines indicate multi-zone model reaction variations that significantly affect the light curve (upper panel) and composition of the burst ashes (lower panel). The thick blue lines indicate reaction rates that were varied in the multi-zone mode but did not lead to significant changes in the respective observable. Note that proton capture flows carry large uncertainties because they are determined from the difference between proton capture and the inverse photodisintegration flows, which both can be very large.